

UC San Diego

UC San Diego Electronic Theses and Dissertations

Title

Structure-function Investigation of Operando Nanostructured Materials Using Coherent X-ray Diffractive Imaging

Permalink

<https://escholarship.org/uc/item/2s75f4q1>

Author

Ulvestad, Andrew

Publication Date

2015

Peer reviewed|Thesis/dissertation

UNIVERSITY OF CALIFORNIA, SAN DIEGO

**Structure-function Investigation of Operando Nanostructured
Materials Using Coherent X-ray Diffractive Imaging**

A dissertation submitted in partial satisfaction of the
requirements for the degree
Doctor of Philosophy

in

Physics

by

Andrew Ulvestad

Committee in charge:

Professor Oleg Shpyrko, Chair
Professor Shirley Meng, Co-Chair
Professor Pao Chao
Professor Patrick Diamond
Professor Stefan Llewellyn Smith
Professor Sunil Sinha

2015

Copyright
Andrew Ulvestad, 2015
All rights reserved.

The dissertation of Andrew Ulvestad is approved, and it is acceptable in quality and form for publication on microfilm and electronically:

Co-Chair

Chair

University of California, San Diego

2015

DEDICATION

To my family, Kasia, Desi, and Syntia for their support throughout
my studies.

EPIGRAPH

I can live with doubt and uncertainty and not knowing. I think it's much more interesting to live not knowing than to have answers that might be wrong.

—Richard Feynman

TABLE OF CONTENTS

Signature Page		iii
Dedication		iv
Epigraph		v
Table of Contents		vi
List of Figures		ix
List of Tables		xii
Acknowledgements		xiii
Vita		xv
Abstract of the Dissertation		xvii
Chapter 1	Introduction	1
	1.1 The case for nanostructured materials	1
	1.2 X-rays	2
	1.3 Scattering by one electron	4
	1.4 Scattering by many electrons	5
	1.5 Crystallography	6
	1.6 Finite Crystals	10
	1.7 Coherence	10
	1.8 Alternative derivation	11
Chapter 2	Coherent X-ray Diffractive Imaging	14
	2.1 Lensless imaging	14
	2.2 Oversampling	15
	2.3 Iterative phase retrieval	16
	2.4 A strained crystal	18
Chapter 3	Electrochemical Energy Storage Devices	20
	3.1 Introduction	20
	3.2 Working principles	21
	3.3 Degradation mechanisms	23

Chapter 4	Nanoscale strain mapping in battery nano structures	25
	4.1 Abstract	25
	4.2 Introduction	25
	4.3 Sample preparation	29
	4.4 Experimental methods	30
	4.5 Results	30
	4.6 Discussion	31
	4.7 Conclusions	34
	4.8 Acknowledgements	35
Chapter 5	Single particle nanomechanics in <i>operando</i> batteries via lens- less strain mapping	36
	5.1 Abstract	36
	5.2 Introduction	37
	5.3 Results	38
	5.4 Sample preparation	44
	5.5 Conclusions	45
	5.6 Acknowledgements	45
Chapter 6	In-situ strain evolution during a disconnection event in a bat- tery nanoparticle	47
	6.1 Abstract	47
	6.2 Introduction	48
	6.3 Experimental Details	50
	6.3.1 Sample Synthesis	50
	6.3.2 Coherent Diffraction Experiment	50
	6.3.3 Phase Retrieval	50
	6.4 Results and Discussion	51
	6.5 Conclusions	56
	6.6 Acknowledgements	57
Chapter 7	Topological defect dynamics in <i>operando</i> battery nanoparticles	58
	7.1 Abstract	58
	7.2 Introduction	59
	7.3 Conclusion	65
	7.4 Acknowledgements	66
Chapter 8	Creating universes with thick walls	68
	8.1 Abstract	68
	8.2 Introduction	68
	8.3 The thin wall revisited	70
	8.3.1 The setup	70
	8.3.2 The two solutions	71

8.4	Visiting the thick wall	72
8.4.1	The turning point	74
8.4.2	The two solutions	75
8.4.3	Results of trying to take $M \rightarrow 0$	75
8.5	Discussion	75
8.6	Conclusion	76
8.7	Acknowledgements	76
Chapter 9	Conclusions	82
Bibliography	84

LIST OF FIGURES

Figure 1.1:	Definition and application of various parts of the electromagnetic spectrum.	3
Figure 1.2:	Plane polarized electromagnetic radiation. An electromagnetic wave contains both the electric and magnetic field.	4
Figure 1.3:	Scattering geometry in a typical experiment. The incident and outgoing vectors are drawn and the path length difference is derived.	6
Figure 1.4:	Geometric derivation of Bragg’s law. Constructive interference occurs when the path length difference is an integer multiple of the wavelength.	7
Figure 1.5:	Lattice and reciprocal lattice for a two dimensional crystal. The reciprocal lattice formulation is especially useful in interpreting the results of scattering experiments.	8
Figure 1.6:	Geometric picture of the scattering condition. Intensity is located at reciprocal lattice points. One sets \mathbf{k}_i and \mathbf{k}_f by choice of sample and detector position.	9
Figure 1.7:	Longitudinal coherence length is defined as the length over which two waves that were in phase take to become π phase shifted.	11
Figure 1.8:	X-ray attenuation coefficient in water. The attenuation coefficient determines the length over which the X-ray intensity falls to $1/e$ of its original value.	12
Figure 2.1:	Sufficiently oversampled diffraction pattern taken at Sector 34-ID-C from a gold nanoparticle. The degree of oversampling is practically given by the number of pixels per fringe.	15
Figure 2.2:	Schematic of iterative phase retrieval The measured data is used as the moduli of the Fourier space image.	16
Figure 2.3:	Displacement field gives rise to an additional path length difference. This path length difference affects the intensity measured in the diffraction pattern.	18
Figure 3.1:	Energy density for various types of batteries. Li-ion are much higher than traditional lead acid batteries.	21
Figure 3.2:	Schematic of battery operation. Lithium ions transfer from the cathode to the anode in conjunction with charge transfer in an external circuit.	22
Figure 3.3:	The spinel intercalation cathode material $\text{LiNi}_{0.5}\text{Mn}_{1.5}\text{O}_4$ and its unit cell. The focus of the X-ray studies presented here will be on spinel structures.	24

Figure 4.1:	(a) Coherent x-rays are produced that illuminate the sample and scatter to give (b) Coherent diffraction pattern from a particular cathode particle, (c) Electron microscopy image of the pristine cathode powder, and (d) Unit cell for the cathode material.	27
Figure 4.2:	Isosurface (25%) projections of strain ($\frac{\partial u_{111}}{\partial x_{111}} \times 10^3$) and displacement (in lattice units) for (a) particle 1 (ex-situ, pristine state) and for (b) particle 2 (in-situ, pristine state) at 50 nm resolution.	32
Figure 4.3:	Cross sections showing the interior distribution of strain in (a) particle 1 and (b) particle 2 at 50 nm resolution.	33
Figure 5.1:	Experimental schematic of the in-situ CXDI setup with lattice constant evolution inset. Diamonds and squares show lattice evolution during discharge and charge, respectively. The scale bar for diffraction data is 0.05 nm^{-1}	39
Figure 5.2:	Isosurface projections of strain evolution. The nanoparticle shell and core both show inhomogeneous strain during discharge. Images are labeled by their respective lattice constant values and open circuit voltages.	40
Figure 5.3:	Interior strain distribution on selected cross-sections at positions shown by the leftmost figure. Single particle strain cross sections show the onset of coherency strain and resulting stripe patterns at 8.143 \AA and 8.142 \AA	42
Figure 5.4:	Elastic energy landscape of a single particle during charge and discharge. Energy barriers to the phase transformation are indicated with green arrows.	44
Figure 6.1:	Schematic of the experimental setup. Coherent X-rays are incident on an in-situ coin cell containing the cathode nanoparticle (green isosurface). Diffracted coherent X-rays are collected on a charge coupled device (CCD).	49
Figure 6.2:	Lattice constant evolution during charging and discharging. In Fig. 2a, the measured lattice evolution is shown in blue circles while the evolution for a connected particle during discharge is shown in dashed X. Fig. 2b shows the open circuit voltage at which the measurements were taken.	51
Figure 6.3:	3D Strain evolution throughout the particle during the disconnection event. Compressive/tensile strain maps before and after the disconnection event are shown for 6 cross-sections located throughout the particle as shown in Fig. 6.2.	54
Figure 6.4:	Total strain energy (fJ) of the single nanoparticle during charging and discharging. Uncertainty is given by the width of the symbols.	56

Figure 7.1:	Bragg coherent diffractive imaging experiment schematic. Coherent X-rays (red) are incident on a cathode nanoparticle (green).	60
Figure 7.2:	Edge dislocation displacement field identified in a single LNMO cathode nanoparticle. Edge dislocations are identified by comparing the measured and predicted displacement field.	61
Figure 7.3:	3D Edge dislocation line evolution due to charging. In Fig. 3A, the evolution of the dislocation line at three different charge states is shown. Fig. 3B shows the same evolution as in Fig. 3A for a different view.	63
Figure 7.4:	The evolution of the local Poisson's ratio as a function of voltage and the proposed auxetic mechanism occurring in the LNMO unit cell. The proposed auxetic re-entrant honeycomb structure is shown in black in Fig. 4C.	64
Figure 7.5:	Displacement and strain dynamics during the onset of the structural phase transformation. Fig. 5A. shows the edge dislocation. Fig. 5B. shows the time evolution of the strain field in the [111] direction $\partial_{111}u_{111}$ at one cross-section higher than in Fig. 5A. Fig. 5C. again shows strain field evolution.	67
Figure 8.1:	A sketch of a bubble solution. A region of de Sitter false vacuum is embedded in a region of true vacuum.	78
Figure 8.2:	A particular ϕ^4 potential with true and false vacuum regions labeled. This potential is used in the numerical solution.	78
Figure 8.3:	T_{00} , a component of the stress energy tensor, demonstrating the wall "thickness", at a given time.	79
Figure 8.4:	Turning point slice of geometry and field for the expanding solution. Here ϕ is dotted, a is dash-dotted, and α is dashed.	79
Figure 8.5:	Turning point slice of the collapsing solution. Here ϕ is dotted, a is dash-dotted, and α is dashed.	80
Figure 8.6:	Mass of the collapsing solution, evaluated at the turning point, as a function of $\Delta\phi$. Points represent a scan of potential parameters λ and γ . Small values of M were not found in the scan.	81
Figure 8.7:	Mass of the collapsing solution, evaluated at the turning point, as a function of ΔV . Points represent a scan of potential parameters λ and γ . Small values of M were not found in the scan.	81

LIST OF TABLES

Table 4.1: Table I. Quantitative strain metrics for the two particles.	33
--	----

ACKNOWLEDGEMENTS

Thank you to my family, extended family, and the village that raised me. Thank you to my advisor for not letting me quit and always financially supporting me. Thank you to the other members of the Shpyrko group for their help with both science and for group therapy sessions.

I'd also like to thank all my collaborators listed below. In particular, Ross Harder and Jesse Clark were always very helpful in explaining coherent imaging and helping me with the phase retrieval code.

Chapter 4, in full, is a reprint of the material Nanoscale strain mapping in battery nanostructures as it appears in Applied Physics Letters, Andrew Ulvestad, Hyung-Man Cho, Ross Harder, Jong Woo Kim, Sebastian Dietze, Edwin Fohntung, Ying Shirley Meng and Oleg G. Shpyrko, 2014, 104, 073108. The dissertation author was the primary investigator and author of this paper.

Chapter 5, in full, is a reprint of the material Single particle nanomechanics in operando batteries via lensless strain mapping as it appears in Nano Letters, Andrew Ulvestad, Andrej Singer, Hyung-Man Cho, Jesse Clark, Ross Harder, Jorg Maser, Ying Shirley Meng and Oleg G. Shpyrko, 2014, 14, 5123-5127. The dissertation author was the primary investigator and author of this paper.

Chapter 6 in full, is a reprint of the material In situ strain evolution during a disconnection event as it appears in Physical Chemistry Chemical Physics, Andrew Ulvestad, Jesse Clark, Andrej Singer, David Vine, Hyung-Man Cho, Ross Harder, Ying Shirley Meng and Oleg G. Shpyrko, 2015, 17, 10551. The dissertation author was the primary investigator and author of this paper.

Chapter 7, in full is currently under review for publication of the material Topological defect dynamics in operando battery nanoparticles. Andrew Ulvestad, Andrej Singer, Jesse Clark, Hyung-Man Cho, Jong Woo Kim, Ross Harder, Jorg Maser, Ying Shirley Meng, and Oleg G. Shpyrko. The dissertation author was the primary investigator and author of this paper.

Chapter 8 in full, is a reprint of the material Creating universes with thick walls as it appears in Physical Review D, Andrew Ulvestad and Andreas Albrecht, 2012, 85, 103527. The dissertation author was the primary investigator and author

of this paper.

I would like to acknowledge the financial support from US Department of Energy, Office of Science, Office of Basic Energy Sciences, under Contract DE-SC0001805 and use of the Advanced Photon Source, an Office of Science User Facility operated for the U.S. Department of Energy (DOE) Office of Science by Argonne National Laboratory, supported by the U.S. D.O.E. under Contract No. DE-AC02-06CH11357. I am also very grateful to the UCSD Interdisciplinary collaboration award and the UCSD Inamori fellowship.

VITA

- 2010 Bachelor of Science in Physics *magna cum laude*, University of California, San Diego
- 2010 Bachelor of Science in Chemical Engineering *magna cum laude*, University of California, San Diego
- 2012 Masters of Science in Physics, University of Chicago
- 2012-2015 Research Assistant, Department of Physics, University of California, San Diego
- 2015 Doctor of Philosophy in Physics, University of California, San Diego

PUBLICATIONS

A. Ulvestad, A. Singer, J.N. Clark, H.M. Cho, J.W. Kim, R. Harder, J. Maser, Y.S. Meng, and O.G. Shpyrko. “Topological defect dynamics in *operando* battery nanoparticles”. *Science* (Revisions submitted).

A. Ulvestad, J.N. Clark, R. Harder, I.K. Robinson, and O.G. Shpyrko. “3D Imaging of Twin Domain Defects in Gold Nanoparticles”. *Nano Letters* (under review).

A. Ulvestad, J.N. Clark, A. Singer, D.J. Vine, H.M. Cho, R. Harder, Y.S. Meng, and O.G. Shpyrko. “*In-situ* strain evolution during a disconnection event in a battery nanoparticle”. *Phys.Chem. Chem. Phys.* , **2015**, 17, 10551-10555

A. Ulvestad, A. Singer, H.M. Cho, J.N. Clark, R. Harder, J. Maser, Y.S. Meng, and O.G. Shpyrko. “Single Particle Nanomechanics in Operando Batteries via Lensless Strain Mapping”. *Nano Lett.*, **2014**, 14 (9), 51235127

A. Ulvestad, H.M. Cho, R. Harder, J.W. Kim, S.H. Dietze, E. Fohtung, Y.S. Meng, and O.G. Shpyrko. “Nanoscale strain mapping in battery nanostructures”. *App. Phys. Lett.*, **2014**, 104, 073108, 26.

A. Ulvestad, A. Albrecht. “Creating universes with thick walls”. *Phys. Rev. D.* **2012**, 85, 103527

A. Singer, **A. Ulvestad**, H.M. Cho, J.W. Kim, J. Maser, R. Harder, Y.S. Meng, and O.G. Shpyrko. “Nonequilibrium Structural Dynamics of Nanoparticles in $\text{LiNi}_{1/2}\text{Mn}_{3/2}\text{O}_4$ Cathode under Operando conditions”. *Nano Lett.* **2014**, 14 (9), 5295-5300

J.W. Kim, S. Manna, S.H. Dietze, **A. Ulvestad**, R. Harder, E. Fohntung, E.E. Fullerton, and O.G. Shpyrko. “Curvature-induced and thermal strain in polyhedral gold nanocrystals”. *App. Phys. Lett.*, **2014**, 105(17), 173108.

ABSTRACT OF THE DISSERTATION

**Structure-function Investigation of Operando Nanostructured
Materials Using Coherent X-ray Diffractive Imaging**

by

Andrew Ulvestad

Doctor of Philosophy in Physics

University of California, San Diego, 2015

Professor Oleg Shpyrko, Chair
Professor Shirley Meng, Co-Chair

Nanostructured devices promise to help solve grand challenges of our time, including renewable energy generation, storage, and mitigating climate change. Their power lies in the particular influence of the surface on the total free energy when dimensions approach the nanoscale and it is well known that different sizes, shapes, and defects can drastically alter material properties. However, this strength represents a considerable challenge for imaging techniques that can be limited in terms of sample environments, average over large ensembles of particles, and/or lack adequate spatiotemporal resolution for studying the relevant physical processes. The focus of this thesis is the development of in situ coherent X-ray

diffractive imaging (CXDI) and its application in imaging strain evolution in battery cathode nanoparticles. Using in situ CXDI, the compressive/tensile strain field in the pristine state is revealed, and found to be linked to a particular concentration of strain inducing Jahn-Teller ions. The evolution of strain during the first charge/discharge cycle shows that the cathode nanoparticle exhibits phase separation. Using the 3D strain field, the strain field energy is calculated and shows interesting hysteresis between charge and discharge. Strain evolution during a disconnection event, in which the cathode nanoparticle is no longer able to exchange electrons and ions with its environment, reveals the formation of a poorly conducting interphase layer. Finally, strain fields were used to study dislocation dynamics in battery nanoparticles. Using the full 3D information, the dislocation line structure is mapped and shown to move in response to charge transfer. The dislocation is used as a way to probe the local material properties and it is discovered that the material enters an “auxetic”, or negative Poisson’s ratio, regime.

Chapter 1

Introduction

1.1 The case for nanostructured materials

Nanoparticles are widely used in materials science across diverse areas including energy storage materials [117], catalysts [74], and sensors [12]. Their desirable characteristics, brought on by decreasing the particle size to the nanoscale, include record catalytic activities [113], improved lithiation kinetics [60], and longer lifespans [22]. Nanoparticle properties are primarily functions of their size, shape and surface facets, and support. For example, shrinking the size of LiFePO_4 cathode nanoparticles improves battery performance [135] while gold and platinum nanoparticle catalytic performance is heavily dependent on the support selection [62, 129]. It was also recently shown that surface facets dramatically impact the performance of $\text{LiNi}_{0.5}\text{Mn}_{1.5}\text{O}_4$ battery cathodes [60]. Thus, in order to truly understand the structure-function relationship, techniques with single particle sensitivities must be employed. Understanding the single particle structure function relationship is further complicated by the additional components in working devices (e.g. binders, additives in batteries) that can change the physics of relevant reaction and the fact that the reactions we aim to optimize (e.g. charge transfer for batteries) occur under far from equilibrium conditions. For example, it was shown that thin films of $\text{LiNi}_{0.5}\text{Mn}_{1.5}\text{O}_4$ are intrinsically stable under high voltage cycling but that electrochemically inactive components contribute to degradation [21]. In LiFePO_4 cathode nanoparticles, there continues to be debate over two-phase co-

existence during the far from equilibrium process of (dis)charging in part because of disagreement between ex-situ and in-situ results [82]. It is thus not enough to study single particles: they must also be studied in their operating environment and ideally under operating conditions.

Motivated by this challenge, researchers are working on several techniques capable of probing single nanoparticles in situ and under operating conditions. In situ electron microscopy was used to understand both the ion distribution in LiFePO₄ cathode nanoparticles [64] and the phase transition in a silicon/carbon anode [131]. Traditional X-ray microscopes are also being employed both in situ and under operando conditions [134]. For a recent review please see [90]. While the aforementioned techniques have certainly improved our understanding on nanoparticles in reactive environments, there are several desirable quantities, the first and foremost strain information, that are difficult to obtain. Strain is known to affect thermodynamic properties at the nanoscale [17, 34, 56, 63]. Strain field information also reveals the location and type of defects that are present, which can significantly alter material properties [20, 118]. This information is thus highly desirable to understand and engineer the structure function relationship in nanoparticles. Finally, many of the previously mentioned microscopes yield only 2D information and are limited to specific sample environments and thicknesses that may not be entirely representative of the real system. Coherent X-ray diffractive imaging is a relatively new tool that can offer 3D strain field evolution in buried nanoparticles in reactive environments. Motivated by the potential for new understanding, we aimed to develop this technique to investigate nanostructured cathodes under operating conditions. First, we review X-rays and the origin of their desirable properties.

1.2 X-rays

Since their discovery in 1895, X-rays have been used as probes of various types of matter by physicists, chemists, physicians, and many others [6]. Their absorption $\sim Z^4$ where Z is the atomic number of the element, which is why bone

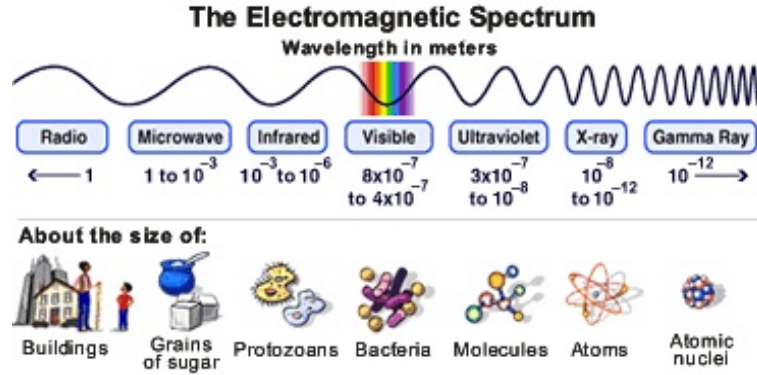


Figure 1.1: Definition and application of various parts of the electromagnetic spectrum.

is visible while skin and tissue are not. X-rays are typically defined as the part of the electromagnetic spectrum having an energy between 100 electron volts (eV) and 100 kiloelectron volts (keV) (see Figure 1.1) with corresponding wavelengths (λ) on the order of .01–10 nanometers, as given by energy-momentum relation for light: $E = hc/\lambda$, where h is Planck’s constant and c is the speed of light. Hard x-rays generally refer to energies above 5 keV and are so-called due to their high penetrating power. As we will see later, this also makes them difficult to focus and led to the advent of “lensless” diffraction microscopy. Their high penetrating power makes them ideal probes for studying operating devices in which the crystal of interest is often buried in other materials [35]. In the case of batteries, which will be discussed later in greater detail, these include a stainless steel casing, lithium metal, organic electrolyte, separator, conductive agent, and a binder. A corollary to hard x-rays’ high energy is their short wavelength. This is important when it comes to imaging, since the best possible resolution is directly proportional to the wavelength. This makes hard x-rays ideal probes for crystals, defined by a repeating structure, which typically have atomic spacings on the order of nanometers.

When these waves interact with matter three things can happen [6]: 1) the X-ray can be absorbed and eject an electron (photo absorption) which is harmful and known as ionizing radiation. This is used for x-ray spectroscopy. 2) The X-ray

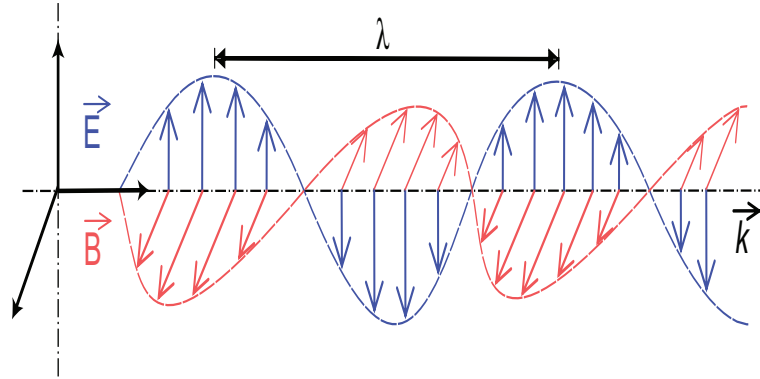


Figure 1.2: Plane polarized electromagnetic radiation. An electromagnetic wave contains both the electric and magnetic field.

can be scattered inelastically (energy not conserved), which is known as Compton scattering. 3) The x-ray can be scattered elastically (Rayleigh scattering) and lose no energy, which means the scattered x-ray has the same frequency as the incoming x-ray. In order to account for both transmission and absorption, one needs the wave equation for X-rays.

1.3 Scattering by one electron

As alluded to previously, X-rays are a form of electromagnetic radiation which can be described as waves (see Figure 1.2). Electromagnetic waves propagate according to Maxwell's equations, which can be reduced to the wave equation for both the \mathbf{E} and \mathbf{B} fields. There is a wonderful derivation in Chapter 1 and Appendices A-B of [6] of the scattering of electromagnetic radiation by electrons, molecules, and crystals, so only key results will be repeated here. The differential scattering cross-section of an electromagnetic wave by a free electron is

$$\left(\frac{d\sigma}{d\Omega}\right) = r_0^2 |\hat{\mathbf{e}} \cdot \hat{\mathbf{e}}'|^2. \quad (1.1)$$

This measures the strength of the outgoing radiation scattered in a certain direction given a quantity of incoming radiation; r_0 is the classical electron radius, which is

the fundamental length scale in the problem; $\hat{\mathbf{e}}$ is the incident polarization while $\hat{\mathbf{e}}'$ is the polarization of the scattered beam (measured at the location of the observer). It is important to note that this equation is independent of X-ray energy, and that it has implications for optimal geometry of different types of X-ray experiments. Synchrotrons produce X-rays with linear polarization in the horizontal plane of the synchrotron. Here, so as to not lose flux from the polarization factor, scattering experiments should be conducted in the vertical plane.

1.4 Scattering by many electrons

One builds up the scattering from crystals by first considering scattering from atoms then scattering from molecules. The electron distribution in an atom is specified by a number density $\rho(\mathbf{r})$, and the scattered radiation is simply the superposition of the contribution from the different scatterers. One wants to know how the volume element at the origin adds with another element at some position \mathbf{r} . The electron density volume element picks up an additional phase from the additional path length difference. From geometry (see Figure 1.3), it is seen that the phase difference between the scattered wave from a volume element around the origin and one around \mathbf{r} is the sums of two terms. The resulting phase difference is thus

$$\Delta\phi(\mathbf{r}) = (\mathbf{k} - \mathbf{k}') \cdot \mathbf{r} = \mathbf{Q} \cdot \mathbf{r}. \quad (1.2)$$

\mathbf{Q} is known as the wave vector transfer or scattering vector. We argue that a volume element $d\mathbf{r}$ at \mathbf{r} contributes $-r_0\rho(\mathbf{r})d\mathbf{r}$ to the scattered field with phase factor $\exp[i\mathbf{Q} \cdot \mathbf{r}]$. The total scattering for an atom is obtained by integrating over all the scatterers:

$$-r_0 \int \rho(\mathbf{r}) \exp[i\mathbf{Q} \cdot \mathbf{r}] d\mathbf{r} \quad (1.3)$$

which is nothing but the Fourier transform of the electron density. This is important for later when discussing phase retrieval algorithms. The intensity measured

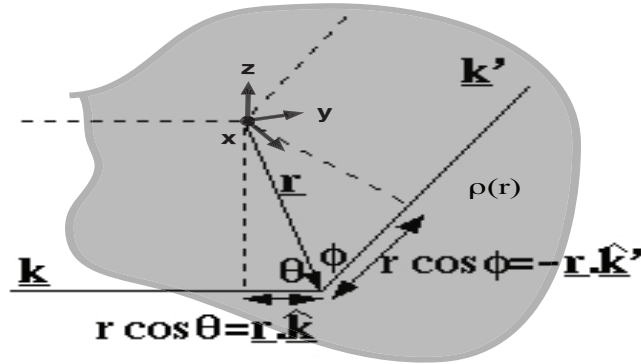


Figure 1.3: Scattering geometry in a typical experiment. The incident and outgoing vectors are drawn and the path length difference is derived.

on the detector is proportional to the absolute value squared of the Fourier transform of the electron density. A molecule is composed of atoms and hence the scattering is a sum over the j atoms

$$F^{mol}(\mathbf{Q}) = \sum_j f_j \exp[i\mathbf{Q} \cdot \mathbf{r}] \quad (1.4)$$

Finally, scattering from a crystal, which is what experiments actually do, requires the introduction of lattice basis vectors and reciprocal lattice basis vectors.

1.5 Crystallography

Crystals are periodic in space, or made up of units (unit cells) that repeat over and over again. Crystals are formed by specifying both a lattice (where the unit cells are) and a basis (the structure of the unit cell). For example, a complex molecule can sit at each lattice point. Consider a simple cubic crystal and the typical derivation of Bragg's law as shown in Figure 1.4. The structure is a crystal and hence has uniform spacing between the blue dots, which could represent atoms or other more complicated structures. The condition for constructive interference is

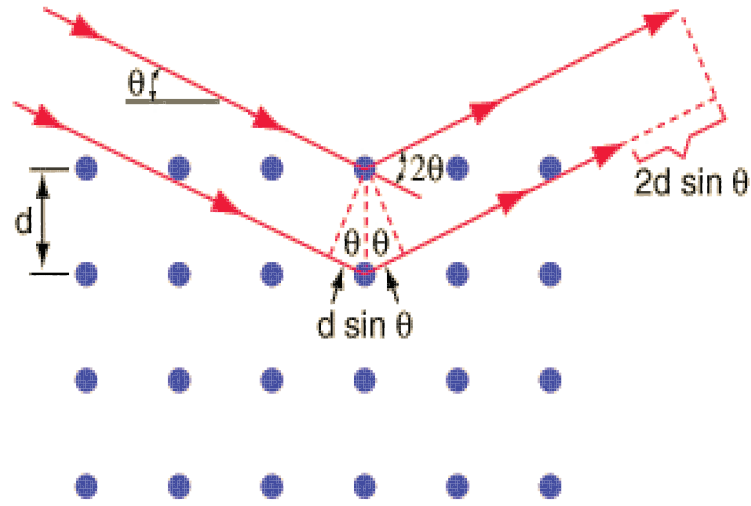


Figure 1.4: Geometric derivation of Bragg's law. Constructive interference occurs when the path length difference is an integer multiple of the wavelength.

$$n\lambda = 2d_{hkl} \sin \theta, \quad (1.5)$$

where d_{hkl} has indices to represent the fact that in phase scattering can happen from different sets of crystallographic planes. To figure out these planes, a real space lattice is first chosen with basis vectors \mathbf{a}_i , not necessarily perpendicular, that can give the positions of all atoms or molecules when they are multiplied by integers. These define the lattice vector

$$\mathbf{R}_n = n_1\mathbf{a}_1 + n_2\mathbf{a}_2 + n_3\mathbf{a}_3 \quad (1.6)$$

A given lattice has characteristic symmetries that lead to “natural” choices for the basis vectors that minimize the volume of the unit cell (see Figure 1.5). Bravais showed that in 2D there are 5 distinct types of lattice symmetries while in 3D there are 14. The combination of the symmetry of the lattice \mathbf{R}_n with the symmetry of the basis \mathbf{r}_j gives 230 possible space groups. Given a lattice and basis, d_{hkl} can be calculated. For example, the (d) spacings of a cubic lattice are

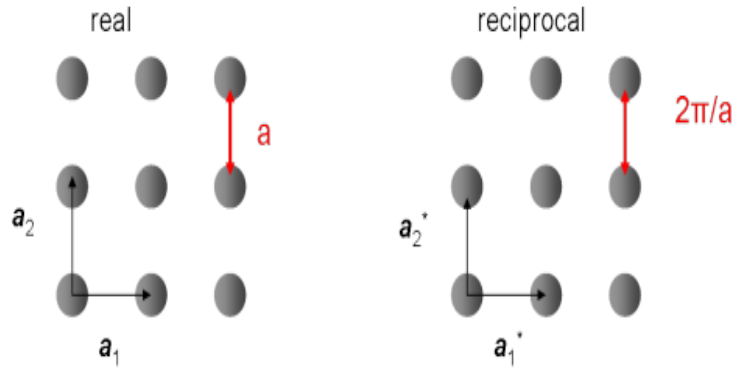


Figure 1.5: Lattice and reciprocal lattice for a two dimensional crystal. The reciprocal lattice formulation is especially useful in interpreting the results of scattering experiments.

$$d_{hkl} = \frac{a}{\sqrt{h^2 + k^2 + l^2}} \quad (1.7)$$

where a is the lattice constant and (h, k, l) are the Miller indices. The Miller indices define the plane from which the scattering occurs. The (h, k, l) plane is defined as the plane closest to the origin that has intercepts $(a_1/h, a_2/k, a_3/l)$. For example, the $(1, 1, 1)$ planes are defined by having their intercepts at $(1, 0, 0)$, $(0, 1, 0)$ and $(0, 0, 1)$.

Now the position of any atom in the crystal is given by $\mathbf{R}_n + \mathbf{r}_j$, so the scattering amplitude factorizes into the product of the “unit cell” and the “lattice”:

$$F^{crystal}(\mathbf{Q}) = \sum_j f_j \exp[i\mathbf{Q} \cdot \mathbf{r}_j] \sum_n \exp[i\mathbf{Q} \cdot \mathbf{R}_n]. \quad (1.8)$$

On average, the phase in the exponential sums to zero unless the scattering vector happens to fulfill

$$\mathbf{Q} \cdot \mathbf{R}_n = 2\pi m \quad (1.9)$$

with m an integer. In order to make the scattering condition more transparent,

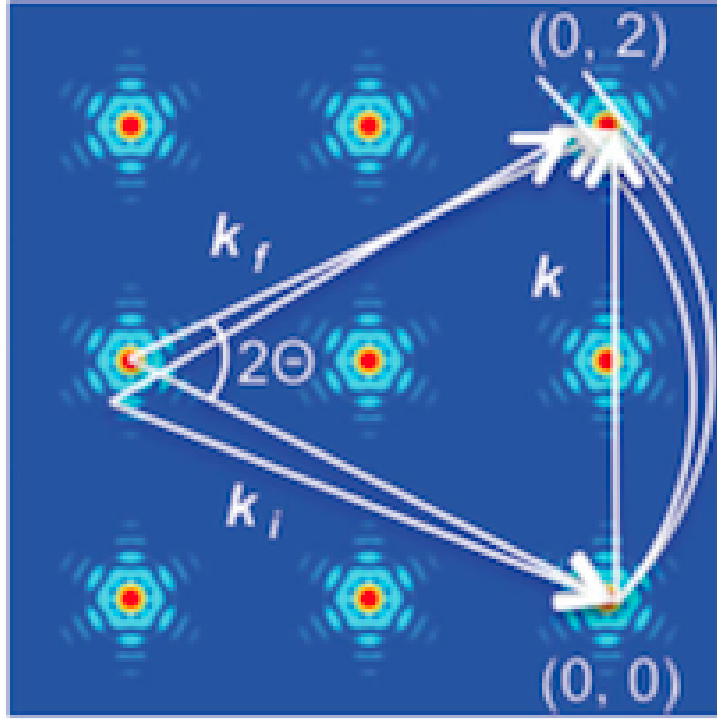


Figure 1.6: Geometric picture of the scattering condition. Intensity is located at reciprocal lattice points. One sets \mathbf{k}_i and \mathbf{k}_f by choice of sample and detector position.

the reciprocal lattice is used. The reciprocal lattice basis vectors \mathbf{a}_j^* are defined such that

$$\mathbf{a}_i \cdot \mathbf{a}_j^* = 2\pi\delta_{ij} \quad (1.10)$$

and the points on the reciprocal lattice are specified by

$$\mathbf{G} = h\mathbf{a}_1^* + k\mathbf{a}_2^* + l\mathbf{a}_3^* \quad (1.11)$$

where the h, k, l are the Miller indices mentioned previously. The lattice can be represented by a periodic function and, provided it is sampled at greater than the Nyquist frequency, all information can be reconstructed by a scattering experiment [105]. Thus there is an intimate connection between a family of planes (h, k, l) in

direct space and \mathbf{G}_{hkl} in reciprocal space. This then satisfies the previous condition that all scattering add in phase when

$$\mathbf{Q} = \mathbf{G} \tag{1.12}$$

which is known as the Laue condition. This is equivalent to Bragg's law discussed previously and has a simple geometric interpretation as shown in Figure 1.6. This implies that scattering is located at discrete points in reciprocal space. These are known as Bragg peaks and are very important as coherent imaging experiments take place in reciprocal space. Thus, given a crystal we can construct a lattice basis, then a reciprocal lattice basis, and then understand exactly where to look for scattering signal. Finally, during all these derivations it was assumed that only a single scattering event took place (kinematical scattering or the Born approximation).

1.6 Finite Crystals

So far we have assumed that crystals were infinite. However, real crystals are finite and hence lead to what is known as “crystal truncation rods” or CTRs. These occur due to the finite size of the crystal. The mathematical description is actually rather simple. The density function is convolved with a step function to represent the truncation. Fig. 5.12 in [6] is an excellent picture. It is important for our measurements as we will see fringes due to the finite size and shape of our crystal.

1.7 Coherence

So far we have assumed that the incoming X-ray was perfectly characterized by a single wavelength λ . Real X-ray beams have a coherence length, which is the distance over which two wavefronts that were in phase become exactly out of phase (see Figure 1.7). The longitudinal coherence length is a measure of how long it

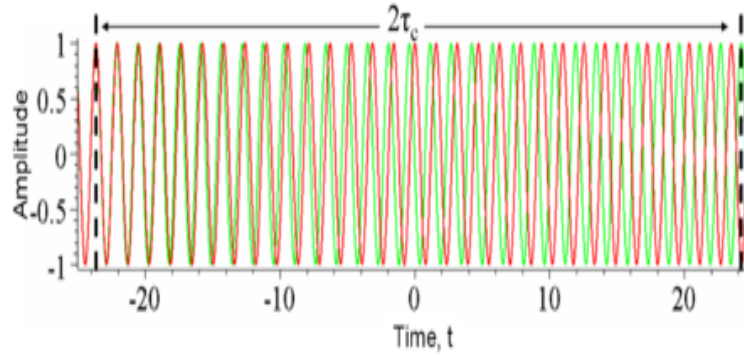


Figure 1.7: Longitudinal coherence length is defined as the length over which two waves that were in phase take to become π phase shifted.

takes two waves that were in phase at some time t to become out of phase. The transverse coherence length is due to the finite size of the source, and is derived considering two waves emitted with different trajectories.

1.8 Alternative derivation

The relationship between scattering and the Fourier transform can be derived as in Pierre Thibault's thesis [120]. Since we ultimately won't worry about polarization factors, the equation we have to solve is the scalar wave equation for Ψ in a medium

$$\nabla^2\Psi + k^2n^2\Psi = 0 \quad (1.13)$$

where $k = \omega/c$ and $n^2 = c^2\epsilon\mu$. ω, c, ϵ and μ are the frequency, speed of light, electric permittivity and magnetic permittivity, respectively. n , also known as the complex refractive index, can be defined as

$$n = 1 + \delta n = 1 - \delta + i\beta$$

The real part ($1 - \delta$) governs the x-ray phase velocity in the material while the imaginary part (β) governs the absorption. n tends to deviate only slightly from

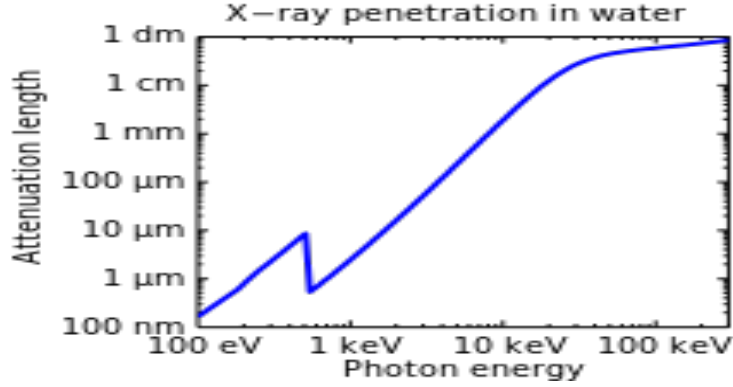


Figure 1.8: X-ray attenuation coefficient in water. The attenuation coefficient determines the length over which the X-ray intensity falls to $1/e$ of its original value.

unity for x-rays due to their high penetrating power and hence is written as $1 + \delta n$. In free space, $\delta n = 0$ and we know the solution is just a traveling wave (Figure 1.2). Note that the form of the equation in Fourier space is

$$(k^2 - \mathbf{q}^2)\tilde{\Psi} = 0 \quad (1.14)$$

which tells us that all Fourier components with $\mathbf{q} \neq k$ are zero. We know this result already from quantum mechanical energy conservation. It is also the result that shows the only nonzero $\tilde{\Psi}$ occur at the Ewald sphere condition ($|\mathbf{q}| = k$).

X-rays are still partially attenuated by matter, however. In order to understand the absorption, we can start with a plane wave propagating in the z -direction through a medium of refractive index n . The intensity of the wave, $I = |\Psi(z)|^2$, is given by $\Psi_0 e^{-\mu z}$ where $\mu = 2\beta k$. This allows us to define the penetration depth as the depth into which the material penetrates before falling to $1/e$ of its initial intensity, or $z = 1/\mu$. The x-ray penetration into water as a function of energy is shown in Figure 1.8.

Let us now discuss 1.13 where we again have negligible matter interaction, $\delta n \neq 0$, and we wish to relate the signal on our detector to the wave field just after it is scattered. There are many ways to derive the result, including using the

Kirchhoff-Fresnel integral and the Born approximation. We can derive the result relevant to our experimental geometry by continuing in the ‘‘Fourier optics’’ formalism and this derivation proceeds as in Thibault thesis. Scattering experiments involve measurement of the wave field in a plane transverse to its propagation direction. As such, we can separate the transverse (r_{\perp}) and parallel (z) components. We then apply the Fourier transform to 1.13 only in these transverse directions, which gives:

$$(-\mathbf{q}_{\perp}^2 + \partial_z^2 + k^2)\tilde{\Psi} = 0 \quad (1.15)$$

One can look up the solution to this equation, which is composed of a forward and backward scattering wave. We are only concerned with the forward scattering solution, which is

$$\tilde{\Psi} = \tilde{\Psi}_f \exp \left[i\sqrt{k^2 - \mathbf{q}_{\perp}^2} z \right] \quad (1.16)$$

The wave evolution is then given at any further z as

$$\Psi = \mathcal{F}^{-1}\tilde{\Psi} \quad (1.17)$$

where \mathcal{F} is the Fourier transform, \mathcal{F}^{-1} is the inverse Fourier transform and now Ψ is a function of \mathbf{r}_{\perp} and z . In order to derive the expression for the diffraction pattern in the ‘‘far-field’’, we take the limit $z \rightarrow \infty$. Writing out the inverse Fourier transform, we have

$$\Psi \rightarrow \mathcal{F}^{-1}\tilde{\Psi} \sim \int d^2\mathbf{q}\tilde{\Psi}(\mathbf{q}) \exp \left[ikz \left(\mathbf{q}/k \cdot \mathbf{r}/z + \sqrt{1 - (\mathbf{q}/k)^2} \right) \right] \quad (1.18)$$

The only non-zero contribution comes when the phase is stationary, which implies $\mathbf{r}_{\perp}/z = \mathbf{q}_{\perp}/\sqrt{k^2 - \mathbf{q}_{\perp}^2}$. So when we measure in the direction $\mathbf{u} = \mathbf{r}_{\perp}/z$ the intensity is

$$I(\mathbf{u}) = |\Psi(z\mathbf{u})|^2 \sim \frac{1}{1 + \mathbf{u}^2} |\tilde{\Psi}(\mathbf{q}_{\perp} = \kappa\mathbf{u})|^2 \quad (1.19)$$

This is the well known result that the far-field intensity is proportional to the square of the absolute value of the 2D Fourier transform. This leads naturally to discussion of the phase problem and of diffraction microscopy.

Chapter 2

Coherent X-ray Diffractive Imaging

2.1 Lensless imaging

In a diffractive imaging experiment, no lens is placed after the sample and only the intensity of the scattered radiation is collected in the far field, typically using a charge coupled device (CCD) camera. It was shown in the previous chapter that this intensity is proportional to the Fourier transform

$$I(\mathbf{u}) = |\Psi(z\mathbf{u})|^2 \tag{2.1}$$

The ultimate goal is to look at the sample in real space by recovering $\rho(\mathbf{r})$. For this to be accomplished, an inverse Fourier transform needs to be performed and thus the Fourier space phases, in addition to the intensity measurements, need to be recovered. Unfortunately our measurement does not accomplish this. Fortunately, a computer can recover the phases in both Fourier and real space provided the experiment meets several conditions.

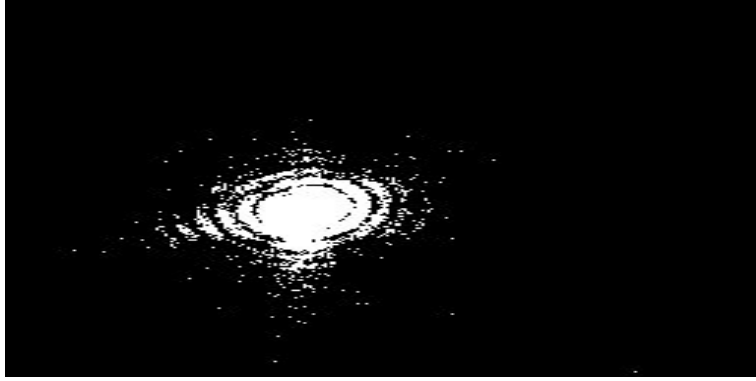


Figure 2.1: Sufficiently oversampled diffraction pattern taken at Sector 34-ID-C from a gold nanoparticle. The degree of oversampling is practically given by the number of pixels per fringe.

2.2 Oversampling

One condition that the recovered phases be unique is in the form of the Shannon sampling theorem, which states that for any signal of frequency f to be recovered with arbitrary accuracy the signal must be sampled with a frequency of at least $2f$. The pre factor of 2 is known as the oversampling ratio. Applying the Shannon sampling theorem to the periodic crystal unit cell, as was first done by Sayre [105], this implies that the diffraction pattern must be oversampled by at least a factor of 2. A useful definition of the oversampling ratio in terms of the computational array is

$$\sigma = \frac{L}{l} \quad (2.2)$$

where L is the number of pixels in the array and l is the number of pixels in the sample. In terms of diffraction images, the oversampling condition translates into having at least 2 pixels per fringe on the CCD. For example, Figure 2.1 is oversampled by at least a factor of 3 because there are more than 3 pixels per fringe. In principle only a factor of 2 is needed, but it appears a higher oversampling speeds the convergence process in retrieving the Fourier space phases.

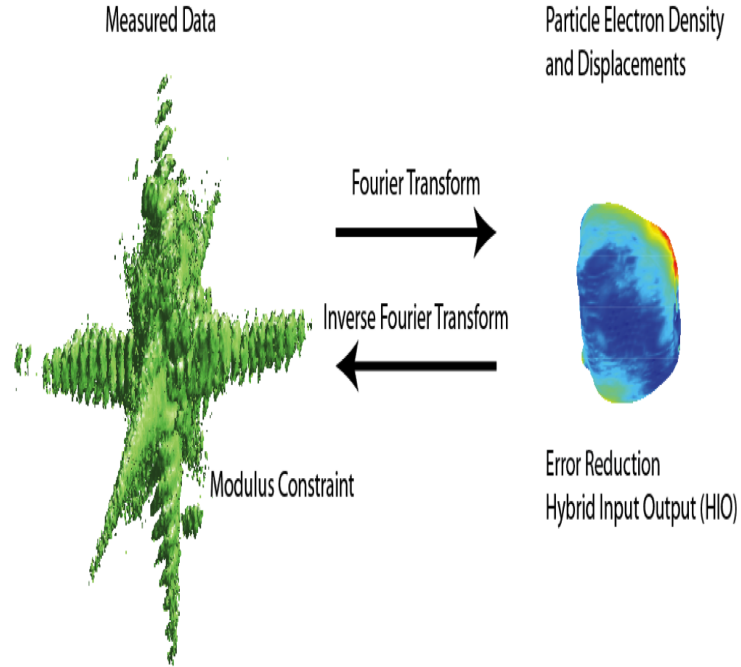


Figure 2.2: Schematic of iterative phase retrieval. The measured data is used as the moduli of the Fourier space image.

2.3 Iterative phase retrieval

As discussed previously, only the intensity of the diffraction pattern is recorded. In order to form the real space image, the phases in Fourier space are needed. Provided the sample is finite (e.g. has compact support), is coherently illuminated, and is smaller than the beam, then the following algorithms will converge to a unique set of phases up to three inherent symmetries of the modulus of the Fourier transform of an arbitrary function $f(x)$.

The symmetries in the Fourier transform include a global phase offset $e^{i\phi_0}$, a complex conjugation plus inversion $f(x) \rightarrow f^*(-x)$, and a rigid shift $f(x) \rightarrow f(x + x_0)$. These are all seen to provide the same Fourier moduli. However, since these do not affect the physical properties of the sample, they are not ultimately important. They are important when performing multiple reconstructions and

averaging the results, as will be shown.

The unique phases can be retrieved using a variety of computation algorithms. The first such algorithm was the Gerchburg-Saxton algorithm introduced in 1972 in electron microscopy, also known as the error reduction algorithm. In this algorithm, the Fourier moduli are measured on the detector. A random set of phases are used to perform the inverse Fourier transform. The object in real space is only kept inside a finite support. The “projected” object is Fourier transformed to Fourier space and the process is repeated. This process mathematically is:

$$|F| = \sqrt{I} \quad (2.3)$$

$$F_i(q) = |F| \exp[i\phi_i] \quad (2.4)$$

$$f_i(x) = \mathcal{F}^{-1}F(q) \quad (2.5)$$

$$f_i(x) = f_i(x) \times h(x) \quad (2.6)$$

$$F_{i+1}(q) = |F| \angle [\mathcal{F}f(x)_{i+1}] \quad (2.7)$$

$$f_{i+1}(x) = \mathcal{F}^{-1}F_{i+1}(q) \quad (2.8)$$

where I is the intensity measurement, ϕ is a set of phases that are initially random, F_i is the best guess of the Fourier transform of the object, f_i is the best guess of the real space object, $h(x)$ is the support function, and \angle represents the imaginary part of the function. The updated guess used at the beginning of the next iteration is f_{i+1} . This algorithm will in principle work given sufficient iterations but in practice is prone to stagnation and slow convergence as monitored by the square of the difference between the measured moduli and the computed moduli, which is known as the error metric.

In order to combat stagnation and slow convergence, a different constraint in real space was proposed by Fienup [48] that uses the following modification for pixels that fall outside the support:

$$f_{i+1}(x) = f_i(x) - \beta f_{i-1}(x) \quad (2.9)$$

where β is the feedback parameter, typically close to unity. Pixels inside the support still obey

$$f_{i+1}(x) = f_i(x) \times h(x)$$

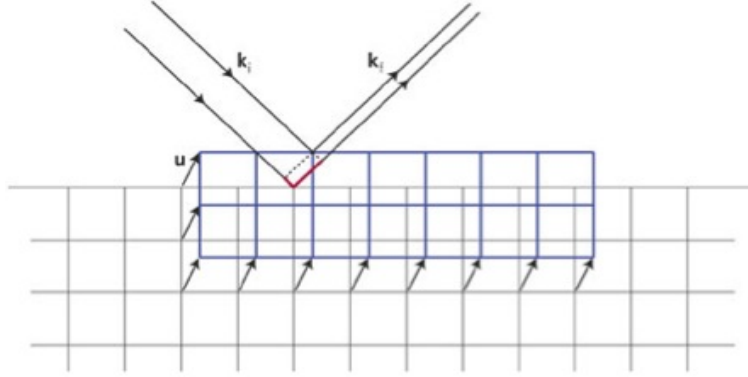


Figure 2.3: Displacement field gives rise to an additional path length difference. This path length difference affects the intensity measured in the diffraction pattern.

This is known as the Hybrid Input-Out (HIO) algorithm. Another significant advance came with the invention of the “shrink-wrap” algorithm, which dynamically evolves the support $h(x)$ [84]. All phase retrieval algorithms can be recast as projection operators as shown in Thibault’s thesis [120].

2.4 A strained crystal

Until now, it has been assumed the finite crystal consisted of a perfect set of repeating unit cells with all atoms at their equilibrium positions. In this case, $\rho(\mathbf{r})$ is real and the resulting Fourier moduli are centrosymmetric. In practice, asymmetries are commonly seen in diffraction patterns that cause the real space image to be complex, e.g.

$$\rho(\mathbf{r}) \rightarrow \rho(\mathbf{r}) \exp[i\chi] \quad (2.10)$$

It turns out that crystal strain is responsible. Consider a displacement field $\mathbf{u}(\mathbf{r})$ as shown in Figure 2.3 (adapted from [102]). The effect of displacement is to add an additional path length difference or phase between the incoming and outgoing radiation. It can be shown that this additional phase χ is equal to the projection of the displacement field onto the measure reciprocal lattice vector

$$\chi = \mathbf{G} \cdot \mathbf{u}(\mathbf{r}) \quad (2.11)$$

For example, if the 111 reciprocal lattice peak is measured then the phase in the real space image will be $\chi = G_{111}u_{111}$. $G_{111} = 2\pi/d_{111}$ and d_{111} known from the unit cell of the system. Thus at for every pixel the magnitude of the displacement in the [111] direction is obtained. To obtain strain, the derivative with respect crystallographic directions can be taken, e.g. $\partial_{x_{111}} u_{111}$ is the compressive/tensile strain in the [111] direction.

Now that the real space density and phases can be recovered and correctly interpreted, it is time to discuss the principles of battery operation.

Chapter 3

Electrochemical Energy Storage Devices

3.1 Introduction

Electrochemical storage devices or batteries are ubiquitous today as a convenient means of storing energy and power devices. Lithium is the primary intercalation ion used given its high electropositivity, or its tendency to easily give up an electron. This leads to a high specific energy as shown in Figure 3.1 (adapted from [117]), power, reversibility, and low self discharge. Energy density is the most important metric for grid storage applications while transportation requires high power. Using Ohm's law

$$V = IR,$$

where V is the voltage, I is the current, and R is the resistance. Combined with the definition of power, p ,

$$p = IV,$$

it is seen that an equivalent definition of power is

$$p = V^2/R,$$

which shows that high voltage batteries are much more powerful than lower voltage batteries due to the square scaling.

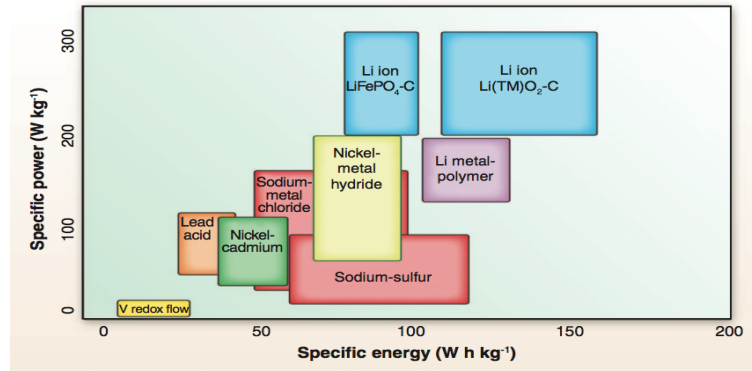


Figure 3.1: Energy density for various types of batteries. Li-ion are much higher than traditional lead acid batteries.

3.2 Working principles

During operation, batteries work as shown in the schematic Figure 3.2 (adapted from [24]). The particular example shown is for Li ion but the principles apply to all batteries. A battery is made up of an anode, electrolyte, and a cathode. The anode is known as the negative electrode and is typically composed of carbon. When the battery is fully charged, all Li ions reside in the anode. The cathode, or positive electrode, is typically a form of transition metal oxide, for example LiCoO_2 in common laptop batteries. During charging, Li ions are pulled out of the cathode and shuttled to the anode. During discharging, the reaction is thermodynamically favorable and thus spontaneous, with Li ions flowing back to the cathode and the electrons performing work on the external circuit.

The reaction at the cathode can be written as



The reaction at the anode can be written as



These two reactions, each one of them called a “half-cell”, combine to give the overall reaction



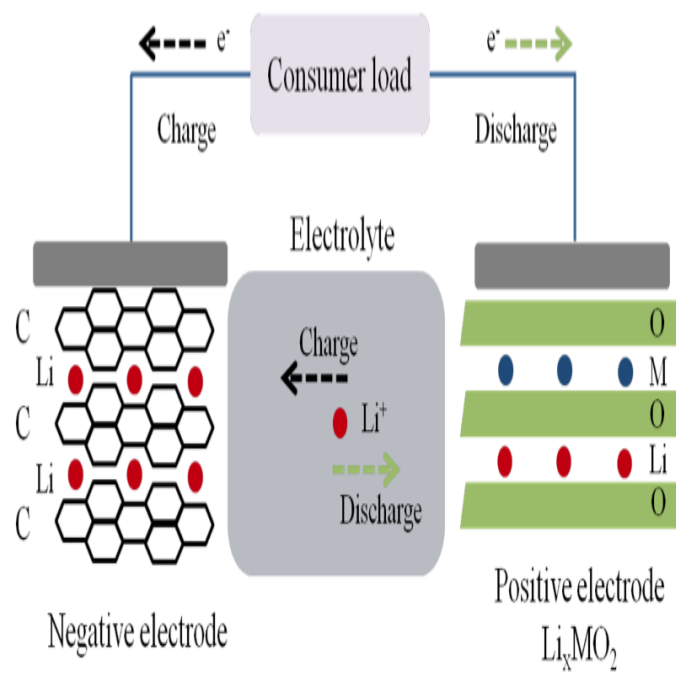


Figure 3.2: Schematic of battery operation. Lithium ions transfer from the cathode to the anode in conjunction with charge transfer in an external circuit.

which gives a corresponding change in the Gibbs free energy, ΔG , of

$$\Delta G = -nF\Delta E, \quad (3.4)$$

where F is Faraday's constant. Thus the thermodynamic driving force is linear in both the difference in standard cell potentials and the moles of electrons transferred. The standard cell potentials are available in a table so given a combination of elements one can compute the theoretical Joules per mol of reaction and thus convert to theoretical energy density. Finally, the Nerst equation relates the measurable cell voltage to the chemical difference across the electrochemical cell via

$$E = -\frac{RT}{nF} \log \frac{a_i^+}{a_i^-}. \quad (3.5)$$

3.3 Degradation mechanisms

The X-ray technique discussed previously is adept at resolving displacement and thus strain fields inside nanoparticles. The degradation mechanisms in batteries that we will thus probe will be strain induced. The particular type of battery we study will be Lithium ion, with a positive cathode of $\text{LiNi}_{0.5}\text{Mn}_{1.5}\text{O}_4$. This is what's known as an intercalation compound. Ions intercalate and deintercalate into the cathode structure causing differential lattice expansion and strain. The unit cell showing the position of all the different types of atoms in the spinel structure is shown in Figure 3.3.

This cathode material also happens to crystallize as a spinel structure, which is cubic with additional symmetries. The primary benefit of the spinel structure are the three-dimensional diffusion pathways that allow easy lithium ion transport into and out of the cathode. Despite these three-dimensional pathways, strain evolution in these compounds is still a problem and limits their applicability in electric vehicles [135, 24].

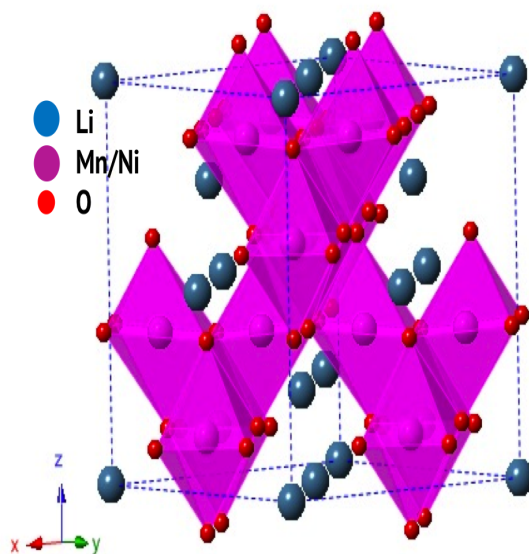


Figure 3.3: The spinel intercalation cathode material $\text{LiNi}_{0.5}\text{Mn}_{1.5}\text{O}_4$ and its unit cell. The focus of the X-ray studies presented here will be on spinel structures.

Chapter 4

Nanoscale strain mapping in battery nano structures

4.1 Abstract

Coherent x-ray diffraction imaging is used to map the local three dimensional strain inhomogeneity and electron density distribution of two individual $\text{LiNi}_{0.5}\text{Mn}_{1.5}\text{O}_{4-\delta}$ cathode nanoparticles in both ex-situ and in-situ environments. Our reconstructed images revealed a maximum strain of 0.4%. We observed different variations in strain inhomogeneity due to multiple competing effects. The compressive/tensile component of the strain is connected to the local lithium content and, on the surface, interpreted in terms of a local Jahn-Teller distortion of Mn^{3+} . Finally, the measured strain distributions are discussed in terms of their impact on competing theoretical models of the lithiation process.

4.2 Introduction

The reduction of battery capacity after many charge/discharge cycles is a well known, yet poorly understood, phenomenon affecting battery performance in a wide range of devices, including cell phones, computers, and electric vehicles [93, 7, 85]. Even the ubiquitous lithium ion battery, which has several desirable

properties [89], suffers under repeated cycling [11]. A detailed understanding of the various processes thought to be involved would shed light on ways to increase longevity and maintain capacity for a larger number of cycles in both current and next generation batteries.

Possible mechanisms for the degradation of battery capacity include unwanted side reactions, electrolyte decomposition, surface film formation, active material dissolution, and structural change [11]. Lithium ions are inserted and removed from both electrodes as the battery is cycled. This causes volume expansion and contraction in a wide range of materials, including spinels, and can occur inhomogeneously, which induces strain in the active material particles [25, 57]. This strain can cause irreversible cracking if it is above the threshold tensile strength of the material [30, 144]. Cracking may lead to disconnection of some active material from the conductive matrix. Strain clearly plays a key role in battery performance and capacity retention.

Although other methods can provide globally averaged strain information [46, 88], improvements in performance will likely require understanding strain at the single particle level. Individual particle information leads, potentially, to a better understanding of how the ensemble functions. If a particular size and shape of particle exhibits minimal strain upon cycling, this can motivate improvement in synthesis techniques to produce a cathode composed of this specific particle. From a fundamental point of view, how phase transitions happen at the single particle level remains unexplored.

Spinel materials are attractive candidates for cathodes in future commercial batteries due to their specific energy, cost, availability, and electrode potential [41, 59, 89]. In general, the spinel structure enhances solid state lithium ion transport because it is based on a three dimensional MO_2 (M: transition metals) host. The pathway relies on vacancies in the transition metal layer along the (111) direction. In the LiM_2O_4 spinel structure, M cations occupy the octahedral site but $\frac{1}{4}$ are located in the lithium layer along the (111) direction, which leaves $\frac{1}{4}$ of the sites in the transition metal layer vacant [119]. Lithium ions then occupy the tetrahedral sites in the lithium layer, and these sites share faces with the empty octahedral

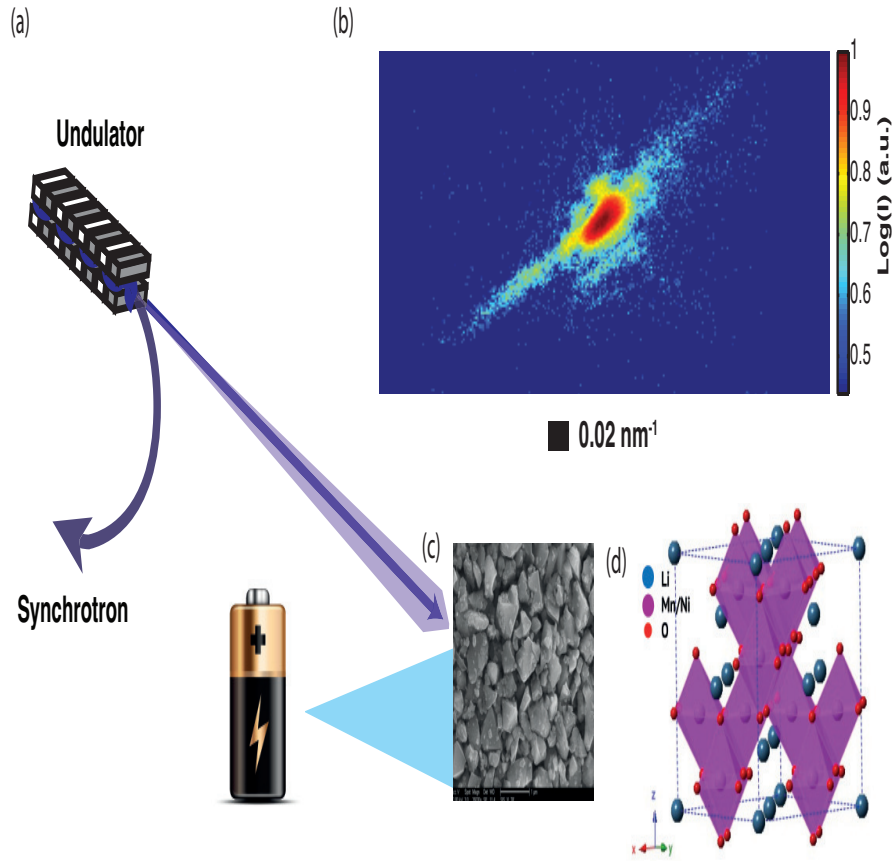


Figure 4.1: (a) Coherent x-rays are produced that illuminate the sample and scatter to give (b) Coherent diffraction pattern from a particular cathode particle, (c) Electron microscopy image of the pristine cathode powder, and (d) Unit cell for the cathode material.

sites in the metal layer [139].

$\text{LiNi}_{0.5}\text{Mn}_{1.5}\text{O}_{4-\delta}$ (LNMO) is the particular type of lithium oxide spinel studied in this experiment where $\delta \approx 0.1$ indicates the degree of disorder and the amount of oxygen vacancies. The unit cell for the disordered structure is shown in Figure 4.1. X-ray diffraction (XRD) data, charge-discharge curves, and differential capacity (dQ/dV) plots are included in supplementary information uploaded with this thesis (Fig. 1s, 2s (a) and 2s (b) respectively). XRD data demonstrates that the structural properties agree with previously published data [137, 72], while charge-discharge and differential capacity curves indicate good electrochemical per-

formance and typical behavior [137, 72]. Strain in these materials can come from a variety of sources, including inhomogeneous lithiation, Mn^{3+} ions undergoing a Jahn-Teller distortion, and the lattice mismatch induced during the structural phase transition that occurs upon cycling [72, 73]. Modeling the lithiation process is typically done by considering spherical particles and assuming homogeneous lithiation across shells [29]. Unfortunately, there are not many experimentally determined strain distributions with which one can compare the model thus these assumptions are left unchallenged.

Coherent x-ray diffractive imaging (CXDI) in Bragg geometry is a powerful characterization technique for imaging local nanoscale lattice distortions [52, 53, 100]. CXDI is fundamentally different than other forms of microscopy. Instead of using a lens to form the image of the sample, the method relies on highly coherent sources of x-rays and the remarkable sensitivity of the scattered coherent beam to the internal structure of the sample. In CXDI the coherently scattered light, or coherent diffraction pattern as shown in Figure 4.1, is directly measured in the far field on an area detector such as a Charge Coupled Detector (CCD). Since only the intensities of the scattered wave can be measured, and not the relative phases of the beams, computational phase retrieval algorithms are employed to generate the image [48].

The strain in the sample will manifest itself in the diffraction pattern as an asymmetry of the coherent diffraction intensities around the Bragg peak of the lattice. An asymmetrical Fourier transform implies a complex real space image. The amplitude will be directly interpreted as the density distribution of the sample, while the phase can be shown to be directly related to a projection of the local lattice distortion onto the G_{hkl} vector of the Bragg peak which was measured [100, 23, 87, 96]. The strain is defined as the gradient of this displacement. In principle, three independent Bragg reflections are necessary to construct the full strain tensor. In this experiment, only the (111) reflection is measured and thus only three components of the strain tensor can be computed.

The phase problem in CXDI is similar in nature to the famous phase problem of x-ray crystallography [105]. An important difference in CXDI is the ability

to oversample the diffraction pattern of the sample in reciprocal space. This fact allows many more constraints to be employed in the phasing retrieval process [48]. The basic concept in phase retrieval is to iterate between real and Fourier space, using a Fast Fourier Transform (FFT), and apply the appropriate constraint in each space. In Fourier space the constraint is simple: the amplitude is set to the measured amplitude, which is the square root of the measured CCD intensity. The real space constraint depends on what algorithm is chosen. Fienup's Hybrid Input-Output (HIO) [48] and the Error Reduction (ER) algorithm were used here. This procedure is done iteratively until it converges on a solution, defined by the error metric, which consists of amplitudes and phases for both spaces.

Several checks were done on the reproducibility and robustness of the phase reconstructions. The diffraction data were centered via a sub-pixel shift to the (h,k,l) of the center of mass of the measured intensity. Each individual particle was reconstructed many times, each with a different set of random phases, and what is shown is the average of at least 5 algorithm solutions. The phase at the reconstructions center of mass is set to zero to remove any global phase offset. The Fourier space error metric, which is the sum square of the deviations of the reconstructed amplitudes from the measured, was on the order of 10^{-3} . Finally, a coordinate transformation back to the lab frame was performed to simplify computation of the compressive/tensile strain.

4.3 Sample preparation

$\text{LiNi}_{0.5}\text{Mn}_{1.5}\text{O}_{4-\delta}$ spinel materials with the disordered structure were synthesized using the sol-gel method. The sol solution was prepared from the stoichiometric mixture of $\text{Ni}(\text{CH}_3\text{COO})_2 \cdot 4\text{H}_2\text{O}$ (Aldrich), $\text{Mn}(\text{CH}_3\text{COO})_2 \cdot 4\text{H}_2\text{O}$ (Aldrich), and $\text{LiOH} \cdot 2\text{H}_2\text{O}$ (Aldrich) in distilled water. Aqueous solution of citric acid was added drop-wise to the mixture with continuous stirring. The pH of the solution was adjusted to 7 by adding an ammonium hydroxide solution. After gel formation at 70°C with vigorous stirring, the precursor was further dried in a vacuum oven overnight. The resulting gel precursors were decomposed at 500°C for 12

hours in air and then calcinated at 900 °C for 14 hours in air. Typical morphology of the $\text{LiNi}_{0.5}\text{Mn}_{1.5}\text{O}_{4-\delta}$ spinel materials with the disordered structure are shown Figure 4.1. The average particle size was about 700 nm with a range of 400–1000 nm.

4.4 Experimental methods

The experiment was performed at 34-ID-C of the Advanced Photon Source (Argonne National Laboratory). A double crystal monochromator was used to select 8.919 keV x-rays with 1 eV bandwidth, and longitudinal coherence length of about $0.7\mu\text{m}$. Slits were used to select a coherent fraction of the beam from the synchrotron that was then focused to about $1.0\mu\text{m}^2$. The pristine spinel powder was mixed with an equal volume solution of duco cement and then held in place on kapton tape for the ex-situ experiment (particle 1). For the in-situ experiment (particle 2), a modified coin cell was used that does not change the sample environment. The CCD detector was oriented at an arbitrary (111) direction corresponding to a 2θ of $\approx 18^\circ$. The sample was then scanned across the beam until a particle satisfying the Bragg condition illuminated the detector.

Coherent diffraction patterns were recorded for the rocking curve of the (111) Bragg reflection by rotating the sample through the Bragg condition in increments of about 0.01 degrees. In our experiment, a CCD detector with $20\mu\text{m}$ pixel size was used to collect the 2D diffraction slice for 40 slices. Full 3D diffraction patterns were then constructed by stacking these 2D frames together.

4.5 Results

The reconstructed real space maps of electron density, lattice displacement, and compressive/tensile strain in the (111) direction for the two different particles are shown in Figure 4.2. Particle 1 is approximately 700 nm in the largest dimension and imaged in an ex-situ environment. Particle 2 is approximately 400 nm in diameter and imaged in an in-situ coin cell environment. The surface is drawn by

specifying a constant value of electron density at 25% of the maximum. Particle cross sections displaying the interior strain distribution are shown in Figure 4.3. The resolution of these maps, calculated geometrically from the maximum momentum transfer we measure and verified by computation of the phase retrieval transfer function [121, 23], is approximately 50 nanometers (nm). The root mean square strain values are displayed in Table 4.1 for the center (150 nm sphere), surface (150 nm shell), and entire particle.

4.6 Discussion

The reconstructed maps provide insight into the structure and strain of pristine (fully lithiated, uncharged) $\text{LiNi}_{0.5}\text{Mn}_{1.5}\text{O}_{4-\delta}$ cathode. The origin of strain in these particles is not well understood and can come from a variety of effects. We rule out particle-particle electrochemical interaction because measurements were made at open circuit voltage (O.C.V.) in which the particles do not exchange lithium with their neighbors, or we would observe current flow. There are residual strains from the manufacturing of these particles but we expect them to be small based on our atomic resolution microscopy image which shows well aligned atomic columns.

In spinel materials, inserting lithium expands the lattice constant, while removing lithium compresses the lattice constant. Provided this is the dominating effect in the strain distribution, the compressive/tensile component of the strain then represents a map of lithium dense and lithium sparse regions. We see in Figure 4.2 that the strain is not homogeneous over the surface of either particle, which would support the so-called phase field models of lithium insertion [109] and not favor bulk diffusion limited “shrinking core” models.

Both particles also display differences between their strain and their displacement. Although atoms in particle 2 are displaced further from equilibrium, the overall strain is lower compared to particle 1. Differences in the particle strain distributions come from a number of effects, including size differences, sample environment differences, and shape differences. Although we cannot untangle all the

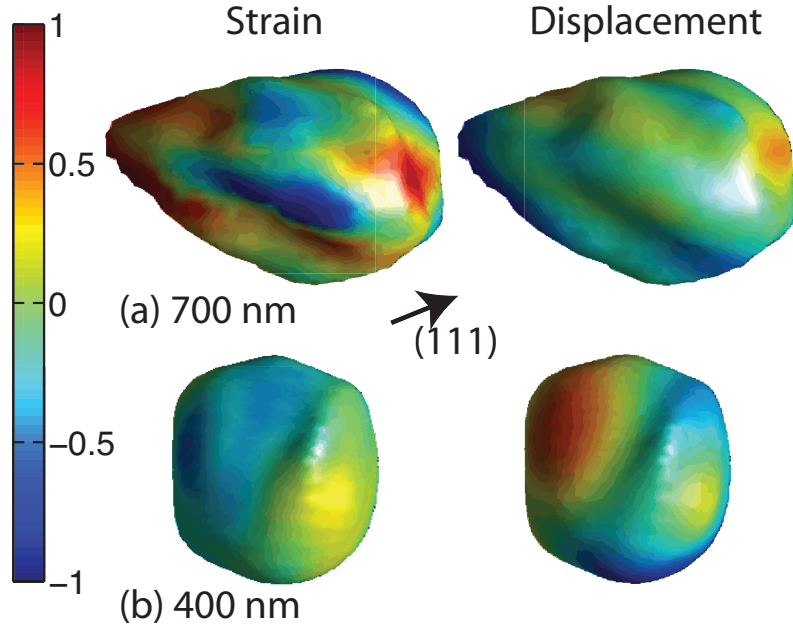


Figure 4.2: Isosurface (25%) projections of strain ($\frac{\partial u_{111}}{\partial x_{111}} \times 10^3$) and displacement (in lattice units) for (a) particle 1 (ex-situ, pristine state) and for (b) particle 2 (in-situ, pristine state) at 50 nm resolution.

effects here, the more symmetric particle (2) is less strained on the surface. Cross sections showing the interior distribution of compressive/tensile strain in particles 1 and 2 are shown in Figure 4.3. We see immediately that the smaller, more symmetric particle 2 is much more homogeneous in terms of strain than particle 1. Assuming, again, that lithium insertion is the dominating effect in the strain of the pristine state, we see that the particles really are inhomogeneously lithiated. These maps, as well as those in Figure 4.2, help us visualize the effects of size, shape, and lithium content on the strain in these cathode particles. This full three dimensional information can be used to determine, quantitatively, the amount of strain in any region.

Table I shows the root mean square strain for the total particle as well as for center (150 nm sphere) and surface (150 nm shell) regions. Both particles display the same feature: surface strain is higher than central strain. We expect surface effects to be important in nano particles and we see evidence of that here. Surface

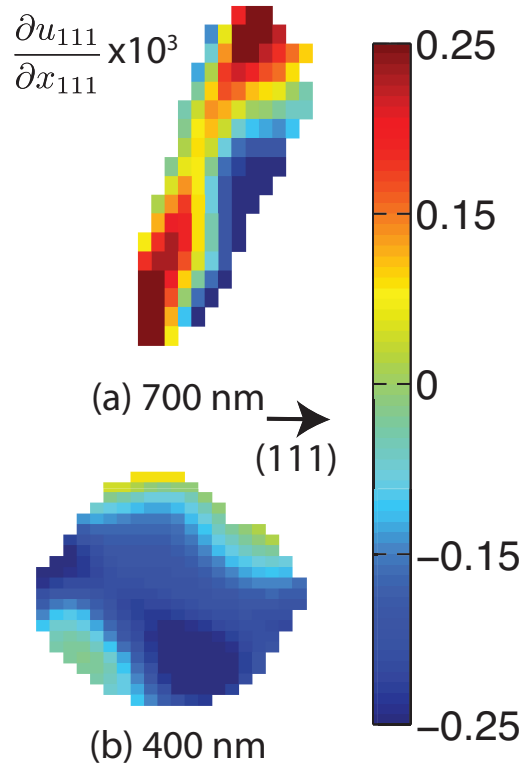


Figure 4.3: Cross sections showing the interior distribution of strain in (a) particle 1 and (b) particle 2 at 50 nm resolution.

Table 4.1: Table I. Quantitative strain metrics for the two particles.

Particle	Total Strain	Center Strain	Surface Strain
1, ex-situ	1.02×10^{-5}	2.21×10^{-4}	3.79×10^{-4}
2, in-situ	1.25×10^{-5}	1.97×10^{-4}	2.07×10^{-4}

strain in these particular type of particles is connected to Mn^{3+} on the surface, produced by high calcination temperature [92]. As mentioned previously, both simulation [114] and experiment [18] point to the formation of Mn^{3+} , although through different mechanisms.

Mn^{3+} has four 3d electrons, and in a six-coordinated oxygen environment it can undergo what is known as a Jahn-Teller distortion and displace the atom from its equilibrium position [140]. The Jahn-Teller (JT) theorem states that in a nonlinear molecule, if degenerate orbitals are asymmetrically occupied, a distortion occurs to remove the degeneracy and lower the overall energy. Significant distortions occur in d^4 high spin ions octahedral ions, which include Mn^{3+} . Unfortunately, the JT theorem is unable to predict the magnitude of the distortion.

Equal concentrations of Mn^{3+} and Mn^{4+} are observed in LiMn_2O_4 [80]. Introducing Nickel reduces the concentration of Mn^{3+} and improves capacity retention [59, 80]. In our particular sample, we compare the measured discharge capacity to the theoretical capacity and arrive at a relative concentration of 13% Mn^{3+} . We will use this number to calculate the magnitude of the JT effect after making several other assumptions, including: the calculated compressive/tensile strain is due only to the JT effect, the strain from multiple ions acts in a collective fashion and simply adds, and the influence of other atoms in the unit cell on the JT distortion is negligible. Under these assumptions, the percent distortion along the z-direction, $\delta z/z$, is calculated to be 2.6×10^{-4} . This is very small local distortion, as compared to other collective JT distortions, such as the distortion in KCuF_3 which is 5.3×10^{-2} .

4.7 Conclusions

Electron density and (111) displacement maps were retrieved using diffraction data from pristine $\text{LiNi}_{0.5}\text{Mn}_{1.5}\text{O}_{4-\delta}$ cathode in both ex-situ (particle 1) and in-situ (particle 2) experiments at Beamline 34 ID-C at the Advanced Photon Source. We applied CXDI to a real system, and gained insight into the strain in this important class of materials. The compressive/tensile strain, which can

be an indication of the local lithium concentration, was calculated from the gradient of the displacement. These strain maps call into question the assumption of homogeneity across “shells” used in theoretical models. The strain maps also demonstrate how particle shape, size, and environment can shape the strain distribution, which influences electrochemical performance. Strain inhomogeneity in single cathode particles was not documented before. The strain was quantified in terms of the root mean square, and the surface strain can be explained by Mn^{3+} that undergoes a local JT distortion. We are able to calculate the magnitude of this local distortion under a number of assumptions and compare it with a known collective JT distortion of another system.

4.8 Acknowledgements

This work was supported by U.S. Department of Energy, Office of Science, Office of Basic Energy Sciences, under Contract DE-SC0001805 and by the UCSD Chancellor’s Interdisciplinary Award. Use of the Advanced Photon Source, an Office of Science User Facility operated for the U.S. Department of Energy (DOE) Office of Science by Argonne National Laboratory, was supported by the U.S. D.O.E. under Contract No. DE-AC02-06CH11357. The author thanks beam line scientist David Vine and staff at Argonne national laboratory and the Advanced Photon Source. The author thanks Kyler Carrol for useful discussions regarding the properties of lithium oxide spinels.

Chapter 4, in full, is a reprint of the material Nanoscale strain mapping in battery nanostructures as it appears in Applied Physics Letters, Andrew Ulvestad, Hyung-Man Cho, Ross Harder, Jong Woo Kim, Sebastian Dietze, Edwin Fohtung, Ying Shirley Meng and Oleg G. Shpyrko, 2014, 104, 073108. The dissertation author was the primary investigator and author of this paper.

Chapter 5

Single particle nanomechanics in *operando* batteries via lensless strain mapping

5.1 Abstract

We reveal three-dimensional strain evolution of a single $\text{LiNi}_{0.5}\text{Mn}_{1.5}\text{O}_4$ nanoparticle in-situ in a coin cell battery under operando conditions during charge and discharge cycles with coherent x-ray diffractive imaging. We report direct observation of both stripe morphologies and coherency strain at the nanoscale. Our results suggest the critical size for stripe formation is 50 nm. Surprisingly, the single nanoparticle elastic energy landscape, which we map with femtojoule precision, depends on charge versus discharge, indicating hysteresis at the single particle level. This approach opens a powerful new avenue for studying battery nanomechanics, phase transformations, and capacity fade under operando conditions at the single particle level that will enable profound insight into the nanoscale mechanisms that govern electrochemical energy storage systems.

5.2 Introduction

Lithium ion batteries are ubiquitous in mobile devices [9], increasingly used in transportation [9], and promising candidates for renewable energy integration into the electrical grid [40] provided the degradation of electrochemical performance upon use can be understood, mitigated, and ideally eliminated [8]. Central to degradation mechanisms in nanostructured electrodes, which are increasingly used in batteries due to their enhanced functionality, are the nanomechanics of lithium ions, which remains insufficiently characterized at the single particle level under operando conditions [14, 145]. In particular, nanostructured spinel materials such as disordered $\text{LiNi}_{0.5}\text{Mn}_{1.5}\text{O}_4$ (LNMO) are appealing as high voltage, high capacity, environmentally friendly, and low cost cathodes for use in numerous markets [37]. However, capacity loss due to degradation is limiting its current use. Important degradation processes, including active material cracking, disconnection, and impedance increase can be understood in terms of strain evolution at the single particle level. Strain needs to be imagined in-situ under operando conditions in order to provide insight into real processes and mechanisms [131].

Thermodynamic considerations characterize the type of strain induced in particular sections of the voltage profile [66]. A composition dependent voltage indicates a solid solution regime in which (de)insertion kinetics induce strain, which is an indirect probe of lithium concentration [123]. Flat, or composition independent, voltage profiles typically indicate two-phase coexistence [66], which induces strain required to maintain coherent (or semi-coherent) interfaces between the phases, known as coherency strain [19]. Several key material properties can be derived from both the number and width of coherent interfaces formed in a single particle [34], although there is some debate as to the mechanics of two-phase coexistence in several important materials (e.g. LiFePO_4) due to the high elastic energy required [36].

Elastic energy is useful in describing structural two-phase coexistence in battery materials, which is key to understanding degradation due to damage induced by the lattice mismatch [8, 112]. The strain generated during, for example, the cubic-tetragonal phase transformation in LiMn_2O_4 causes irreversible damage,

including defect nucleation, which leads to large capacity fade [8]. Structural transformations can be understood by mapping the elastic energy landscape, i.e. the barrier height and width between the two energy minima. This two-state formalism is ubiquitous, and very successful in describing diverse phenomena including formation of ferromagnetic and ferroelectric domains [107], spinodal decomposition [19], early universe scenarios [124], and simple molecules [54]. Applied to batteries, it could suggest avenues to mitigate phase transformation induced damage.

Nanoscale strain measurement is thus useful in mapping lithium inhomogeneity, determining key material properties, and discerning the energy landscape, provided the full three dimensional information is known. Coherent x-ray diffraction imaging (CXDI) in Bragg geometry is a powerful tool that can provide this strain information at the nanoscale by utilizing interference from coherent x-rays coupled with phase retrieval algorithms to reconstruct the electron density and out of equilibrium displacement of nanocrystals [142, 102, 97, 32]. Recently, we used CXDI to map strain in pristine LNMO cathode particles and discovered inhomogeneous strain distributions that can be explained by a competition between various effects [123].

In this chapter, we elevate CXDI to in-situ, in-operando conditions to study the spatial and temporal strain evolution of a single nanoparticle in a LNMO cathode over the entire voltage profile during (dis)charge. Upon charging, solid solution exists for high lithium content, while multiple cubic phases coexistence for low lithium content [71]. The quantitative impact of each regime on the strain is largely unknown, and the fundamental lithiation mechanism (i.e. core/shell or phase field) is unresolved. Additionally, the spatial and temporal kinetics of the cubic-to-cubic phase transformation are largely unknown. This material thus displays phenomena pertinent to many promising batteries.

5.3 Results

The experimental setup is depicted in Figure 5.1. Focused coherent x-rays are incident on an in-situ coin cell and the signal scattered by an individual LNMO

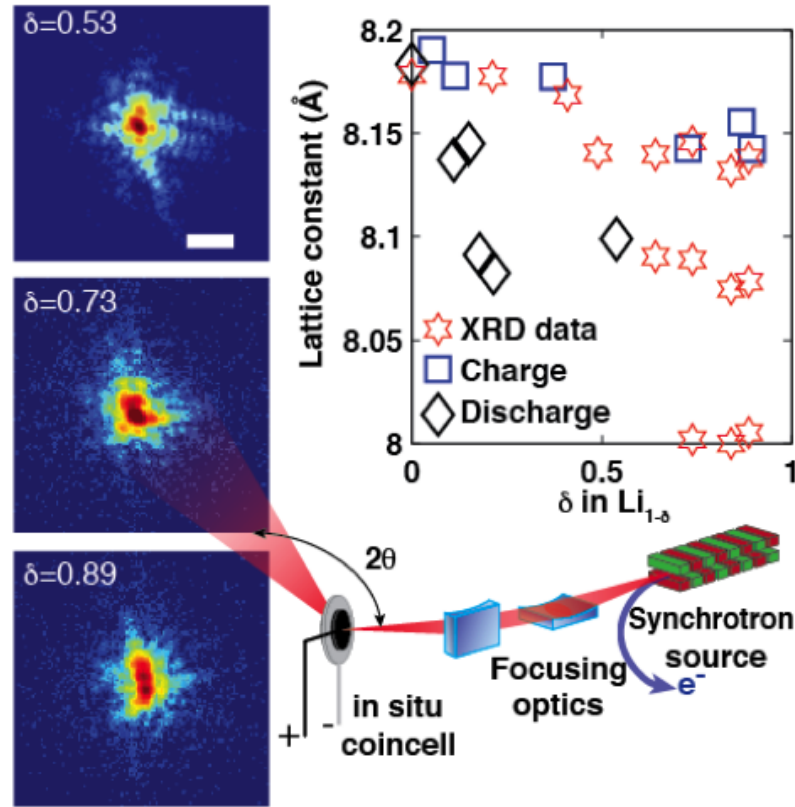


Figure 5.1: Experimental schematic of the in-situ CXDI setup with lattice constant evolution inset. Diamonds and squares show lattice evolution during discharge and charge, respectively. The scale bar for diffraction data is 0.05 nm^{-1} .

particle satisfying the Bragg condition is recorded at the detector. Cross-sections of the (111) Bragg peak show both the central location, which indicates the average lattice constant, and the asymmetry, which indicates strain modulations, change in response to the amount of lithium in the particle [102]. Lattice evolution during charge (squares) is consistent with our ex-situ x-ray diffraction (XRD) measurement (red stars) taken during charge and literature values [71]. We will denote the alpha, beta, and gamma phase as the phases with 8.15, 8.1, and 8.0 lattice constants, respectively, all of which are cubic. During discharge (diamonds) the single particle lattice shows a different behavior compared to XRD data for the beta phase, which is likely due to the decrease in diffusivity at low lithiation and

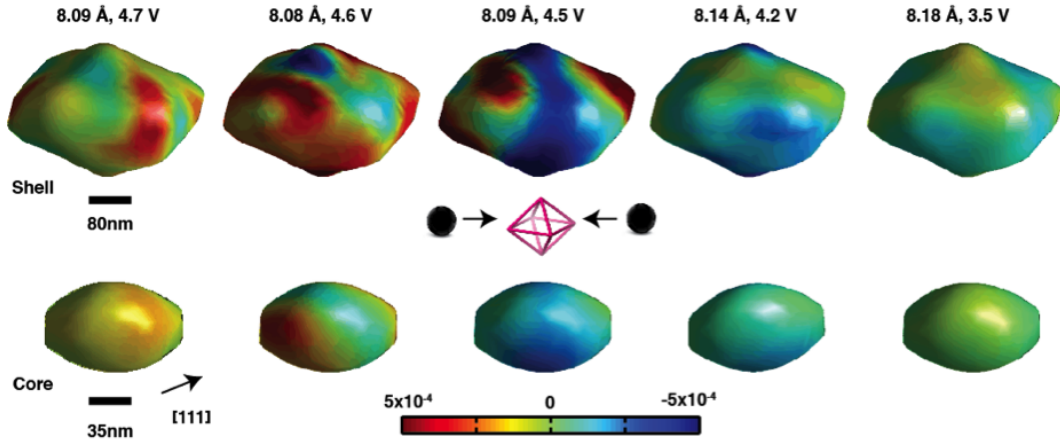


Figure 5.2: Isosurface projections of strain evolution. The nanoparticle shell and core both show inhomogeneous strain during discharge. Images are labeled by their respective lattice constant values and open circuit voltages.

hysteresis between charging and discharging [141]. From the coherent diffraction data, we reconstruct the three-dimensional displacement field u_{111} in an individual cathode particle with 40 nm resolution as defined by the phase retrieval transfer function. The conversion from phase to displacement for each charge state uses the average lattice constant of the particle at that charge state. In the two-phase regions, the initial phase is the reference state. Figure 5.2 displays the compressive (blue) and tensile (red) strain ($\partial_{x_{111}} u_{111}$) evolution on the shell and core as the battery underwent the first discharge at a C/2 rate (2 hours for full discharge). The [111] direction is indicated. A schematic indicates that discharge corresponds to lithium insertion. The particle is octahedral in shape and roughly 400 nm in diameter, which is a size and shape commonly observed using scanning electron microscopy. We use our coherent powder diffraction study to ensure the particle is representative of the average and stable. Effects due to X-ray exposure were confirmed to be negligible by repeated measurements. Note that the voltage is a global measurement while the particle lattice constant is a single particle measurement.

The strain inhomogeneity in Figure 5.2 is striking. Early in the discharge cycle (4.7 V, 8.09 Å), strain manifests itself on the surface in the form of domain-like structures. State 2 (4.6 V, 8.08 Å) shows the onset of coherency strain, which

we expect due to the flat voltage profile and phase coexistence in this region. State 3 (4.5 V, 8.09 Å) shows the strain builds as the particle nears the structural phase transformation, and then finally relaxes after the phase transformation (4.2 V, 8.14 Å). X-ray diffraction data (Figure 5.1) suggests that the material at 8.14 Å (4.2 V) and 8.18 Å (3.5 V) is in the solid solution regime, where compressive/tensile strain correlates to lithium concentration [123]. The strain is clearly inhomogeneous, indicating that phase field models of lithiation [110] are more applicable than core-shell models [28], despite the 3D diffusion pathways in this structure. Strain is minimized at full lithiation (8.18 Å, 3.5 V), as all unit cells are in principle equivalent at this point.

Full 3D strain evolution inside the particle during charging is shown in Figure 5.3 and quite revealing. Beginning with 8.19 Å (3.5 V), we observe competition between pristine state strain and compressive strain at the edges of the particle due to the geometric effect described by the Young-Laplace model [103]. During charge, both 8.143 Å (4.67 V) and 8.142 Å (4.8 V) are in the multiple phase regions of the lattice constant data (Figure 5.1), which indicates two-phase coexistence and thus coherency strain. Two-phase coexistence is confirmed at the single particle level by an in-situ powder diffraction study [108]. To interpret phase separation, we apply the theory developed by Cahn and Hilliard [19]. The free energy of a nonuniform binary solution is

$$F = N_V \int \left((f_0(c) + \kappa(\nabla c)^2 + 1/2 \sum \sigma_{ij} \epsilon_{ij}) \right) dV \quad (5.1)$$

where the local lithium ion concentration, c , is the order parameter of the phase field model, N_V is the number of molecules per unit volume, and $f_0(c) = \Omega c(1 - c) + kT(c \log c + (1 - c) \log(1 - c))$ where Ω, k, T represent the regular solution parameter, Boltzmann constant, and temperature, respectively. The first and second part of $f_0(c)$ are the enthalpic and entropic contributions that favor phase separation and phase mixing, respectively. The second term in equation 5.1 represents the “gradient energy” with coefficient κ . The final term is the sum of the product of the stress and strain tensors, which is the elastic energy. Both the gradient and elastic energy penalize spatial concentration modulation. An initially homogenous, marginally stable mixture governed by equation 5.1 phase separates

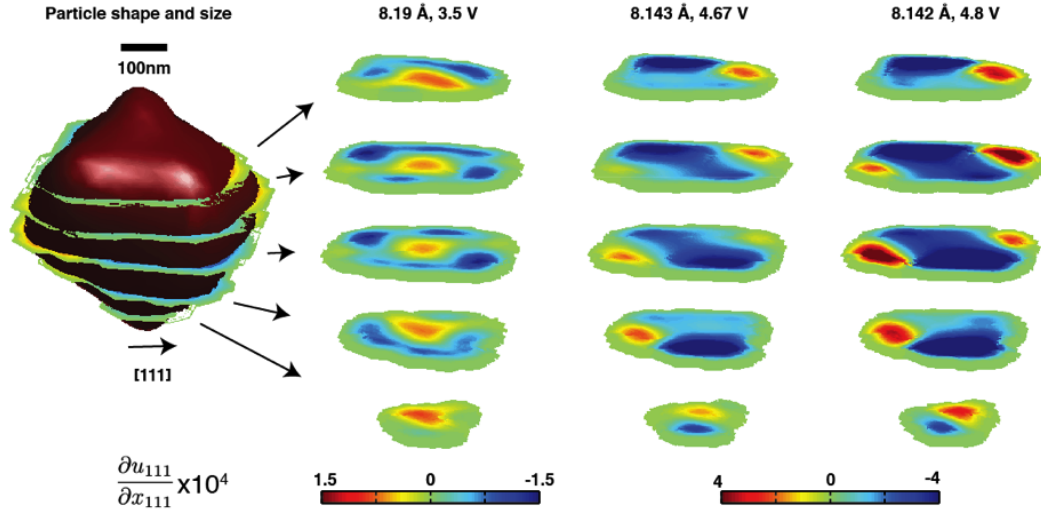


Figure 5.3: Interior strain distribution on selected cross-sections at positions shown by the leftmost figure. Single particle strain cross sections show the onset of coherency strain and resulting stripe patterns at 8.143 Å and 8.142 Å.

under perturbations, despite coherency strain, into a striped morphology that is preferred due to elastic energy relaxation at the particle boundaries [34, 70]. The width of the stripes (see Figure 5.3, 8.143 Å (4.67 V) and 8.142 Å (4.8 V)) can be related to the interfacial energy by a scaling relation [34] derived from minimization of equation 5.1:

$$\lambda = 2w = \sqrt{\frac{2\gamma L_c}{\Delta f}}$$

which implies $\gamma \sim 106$ mJ/m². Here λ is the period of the striping, γ is the interfacial energy, L_c is the width of the particle along which the phase separation occurs, and Δf is the difference in free energy density between the homogeneous and coherent phase-separated state. This interfacial energy is similar to LiFePO₄ [34, 127] and roughly equivalent to the surface tension of water. The diffuse width of the stripe boundary, estimated from the images as 50 nm, provides an estimate for the minimum size for two-phase coexistence [34]. Particles below this size should not phase separate, but exist entirely as one phase or the other. The width

of both the stripes and the interface thus reveal significant information about this LNMO particle.

We also map the elastic energy landscape by utilizing the three-dimensional strain distribution to evaluate the elastic energy which, under isotropic shear-free conditions [19], is

$$E_s = \int (1/2 \sum_{ij} \sigma_{ij} \epsilon_{ij} dV) = (2G + 3I)/2 \int (\partial_{x_{111}} u_{111})^2 dV \quad (5.2)$$

where G and I are the Lamé constants for the material, estimated using molecular dynamics simulations of LiMn_2O_4 spinel [78], and the volume integral is over the entire particle. LNMO always maintains a cubic lattice structure (Figure 5.1) so one strain component is sufficient to evaluate the sum. Elastic strain energy counts the strain due to deviations of the atoms from their equilibrium position, regardless of the underlying cause of the displacement. Figure 5.4 shows the values of the elastic energy, on the order of femtojoules, at different charge states. The mapping of the energy landscape reveals surprising dynamics, including a clear difference in the location, energy, and asymmetry of the energy barrier between charge and discharge (confirmed for another particle). Although hysteresis in a globally averaged variable, such as the voltage, is expected, this hysteresis is at the single particle level and involves the three-dimensional strain field. It is unexpected, and can perhaps be explained by accounting for losses in the form of irreversible elastic energy release via sound waves, cracks, and dislocation nucleation [127]. Electrostatic repulsion may also play a role in determining the height of the energy barrier since it is much greater in the high delta vs. low delta states as observed in diffusion coefficient measurements [141]. Alternatively, the “uphill” diffusion required to form stripes can explain the decrease in effective diffusion coefficients. During discharge, we successfully pushed the particle from the beta phase to the alpha phase. During charge, we believe we were on the cusp of transforming from the alpha phase to either the beta or gamma phase due to the similarity in the strain distributions between the highest strain state during discharge and that during charge. The landscape indicates the phase transformation from large to small lattice constant is much worse in terms of elastic energy per unit cell than the reverse

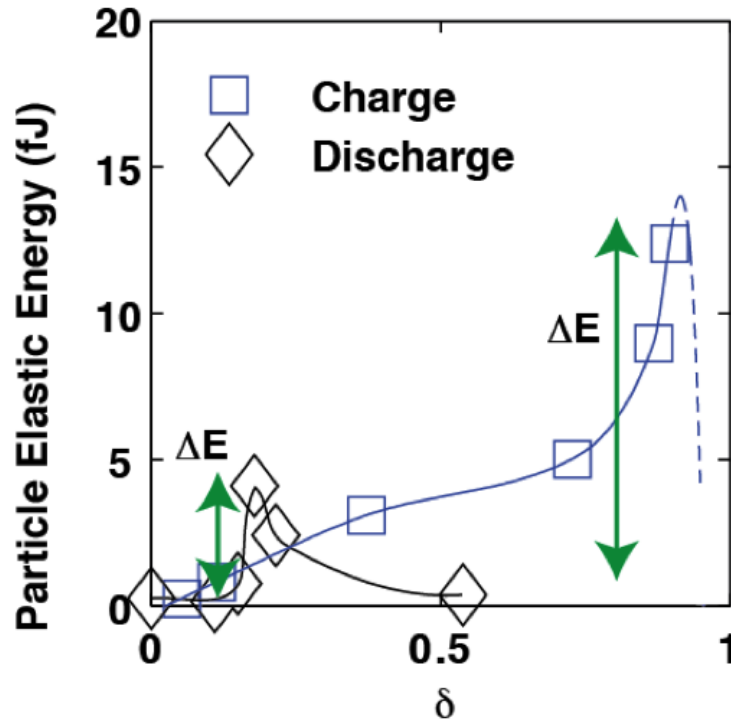


Figure 5.4: Elastic energy landscape of a single particle during charge and discharge. Energy barriers to the phase transformation are indicated with green arrows.

transformation, which must be included in modeling. The map suggests that focusing on ways to minimize the elastic energy, especially upon charge, for example via the creation of more stripes by decreasing the interfacial energy in some way, is of paramount importance in increasing capacity retention and lifetime of LNMO spinel materials.

5.4 Sample preparation

$\text{LiNi}_{0.5}\text{Mn}_{1.5}\text{O}_{4-\delta}$ spinel materials with the disordered structure were synthesized using the sol-gel method. The sol solution was prepared from the stoichiometric mixture of $\text{Ni}(\text{CH}_3\text{COO})_2 \cdot 4\text{H}_2\text{O}$ (Aldrich), $\text{Mn}(\text{CH}_3\text{COO})_2 \cdot 4\text{H}_2\text{O}$ (Aldrich), and $\text{LiOH} \cdot 2\text{H}_2\text{O}$ (Aldrich) in distilled water. Aqueous solution of citric acid was

added drop-wise to the mixture with continuous stirring. The pH of the solution was adjusted to 7 by adding an ammonium hydroxide solution. After gel formation at 70 °C with vigorous stirring, the precursor was further dried in a vacuum oven overnight. The resulting gel precursors were decomposed at 500 °C for 12 hours in air and then calcinated at 900 °C for 14 hours in air. The average particle size was about 700 nm with a range of 400-1000 nm.

5.5 Conclusions

We studied strain evolution in-situ at the single particle level under operando conditions during (dis)charging using CXDI. We discovered a surprisingly rich set of phenomena related to strain formation and propagation, coherency strain and striping, and the evolution of the elastic energy landscape with 40 nm spatial resolution and 0.5 femtojoule energy resolution. Going beyond traditional imaging, we used the strain mapping to determine key material properties, including the minimum size for two-phase coexistence and the interfacial energy, and we mapped the asymmetric energy barrier to the structural phase transformation. This approach unlocks a new, powerful way to conduct in-situ studies under operando conditions of nanomechanics in many electrochemical energy storage systems at the single particle level.

5.6 Acknowledgements

This work was supported by U.S. Department of Energy, Office of Science, Office of Basic Energy Sciences, under Contract DE-SC0001805. H.M.C. and Y.S.M. acknowledge the financial support by U.S. Department of Energy, Office of Basic Energy Sciences, under Award Number DE-SC0002357. O.G.S. and Y.S.M. are grateful to the UCSD Chancellors Interdisciplinary Collaborators Award that made this collaboration possible. Use of the Advanced Photon Source, an Office of Science User Facility operated for the U.S. Department of Energy (DOE) Office of Science by Argonne National Laboratory, was supported by the U.S. D.O.E. under

Contract No. DE-AC02-06CH11357. A.U. thanks beam line scientist David Vine and staff at Argonne National Laboratory and the Advanced Photon Source for their support. J.N.C gratefully acknowledges financial support from the Volkswagen Foundation.

Chapter 5, in full, is a reprint of the material Single particle nanomechanics in operando batteries via lensless strain mapping as it appears in Nano Letters, Andrew Ulvestad, Andrej Singer, Hyung-Man Cho, Jesse Clark, Ross Harder, Jorg Maser, Ying Shirley Meng and Oleg G. Shpyrko, 2014, 14, 5123-5127. The dissertation author was the primary investigator and author of this paper.

Chapter 6

In-situ strain evolution during a disconnection event in a battery nanoparticle

6.1 Abstract

Lithium ion batteries are the dominant form of energy storage in mobile devices, increasingly employed in transportation, and likely candidates for renewable energy storage and integration into the electrical grid. To fulfill their powerful potential, electrodes with increased capacity, faster charge rates, and longer cycle life must be developed. Understanding the mechanics and chemistry of individual nanoparticles under in-situ conditions is a crucial step to improving performance and mitigating damage. Here we reveal 3D strain evolution within a single nanoparticle of a promising high voltage cathode material, $\text{LiNi}_{0.5}\text{Mn}_{1.5}\text{O}_4$, under in-situ conditions. The particle becomes disconnected during the second charging cycle. This is attributed to the formation of a cathode electrolyte interphase layer with slow ionic conduction. The three-dimensional strain pattern within the particle is independent of cell voltage after disconnection, indicating that the particle is unable to redistribute lithium within its volume or to its neighbours. Understanding the disconnection process at the single particle level and the equilibrium

or non-equilibrium state of nanoparticles is essential to improving performance of current and future electrochemical energy storage systems.

6.2 Introduction

Lithium-ion batteries can become the de facto choice for high power energy storage solutions in both transportation and the integrated smart power grid provided the degradation of electrochemical performance during use can be understood, mitigated, and ideally eliminated [9, 8]. Spinel materials such as disordered $\text{LiNi}_{0.5}\text{Mn}_{1.5}\text{O}_4$ (LNMO) are appealing as high voltage, high capacity, environmentally friendly, and low cost cathodes for use in numerous markets [37]. However, capacity loss due to degradation is limiting its current use.

Important degradation effects [111] include active material cracking [28], electrochemical disconnection, and impedance increase due to the formation of electrode electrolyte interphases [130]. Disconnection is an important process as it leads to loss of active material that decreases specific energy and capacity. Disconnection describes the inability of the nanoparticle to exchange electrons with the current collector and/or ions with the electrolyte under externally applied voltage and current. Disconnection is usually explained by a combination of factors, including surface chemistry change, surface layer formation, particle cracking, particle movement, or a failure of contact between the particle and the conductive matrix [95]. However, understanding individual disconnection events is challenging as few techniques provide a direction measure of a particles connectivity while also elucidating strain or ion concentration fields. As such, root causes of disconnection for specific materials are yet to be determined. Electron microscopy [65, 86] and X-ray microscopy [42, 79, 134] are useful tools for understanding degradation in battery nanoparticles, including cracking. However, both suffer from the inability to directly determine with a high degree of accuracy whether or not the damaged particles are still connected. In addition, these techniques do not directly provide strain evolution and specialized sample environments can be required. Here we employ a technique known as coherent X-ray diffractive imaging (CXDI). CXDI

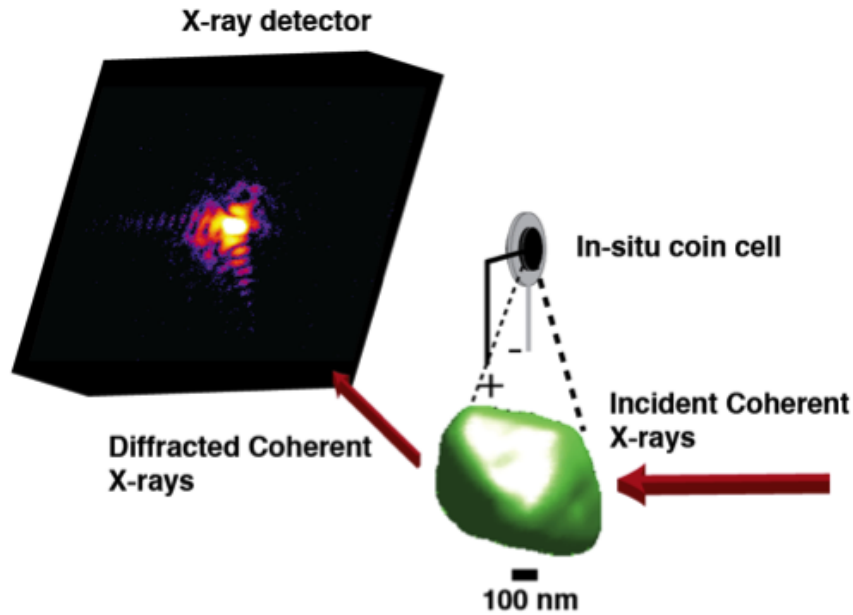


Figure 6.1: Schematic of the experimental setup. Coherent X-rays are incident on an in-situ coin cell containing the cathode nanoparticle (green isosurface). Diffracted coherent X-rays are collected on a charge coupled device (CCD).

in Bragg geometry is a powerful tool that relies on synchrotron produced coherent X-rays and their diffraction from crystalline samples [123, 102, 32, 31, 108]. The 3D electron density and atomic displacement fields are retrievable from coherent diffraction patterns with the use of phase retrieval algorithms [101, 61]. Strain fields are the derivatives of the 3D displacement field components. Due to the high penetrating power of 9 keV X-rays, strain field information under in-situ conditions in real devices can be obtained, ensuring insight into real life processes [131, 64, 134]. 3D strain information is incredibly useful as a local Li concentration probe, in understanding structural dynamics during charge transfer, and in understanding defects and elastic material properties [123].

In Bragg geometry, the sensitivity of the monochromator (10^{-4}) sets the measurement uncertainty in the lattice constant, orientation, and strain of the single particle [133]. In LNMO, the lattice constant varies proportionally with the lithium content, known as solid solution, from 3.5 V (fully discharged) to approximately 4.7 V. Thus measuring the lattice constant during solid solution

provides a direct measure as to the particles connectivity.

6.3 Experimental Details

6.3.1 Sample Synthesis

$\text{LiNi}_{0.5}\text{Mn}_{1.5}\text{O}_4$ disordered spinel was synthesized using the sol gel method [26]. X-ray diffraction data and charge/discharge curves are in good agreement with the literature [71] and confirm both the Fd-3m unit cell structure and expected electrochemical performance. The electrochemical cell consisted of LNMO cathode and lithium metal anode. The electrolyte was a 1M solution of lithium hexafluorophosphate in a 1:1 volume mixture of ethylene carbonate and dimethyl carbonate.

6.3.2 Coherent Diffraction Experiment

A double crystal monochromator was used to select $E=8.919$ keV X-rays with 1 eV bandwidth and longitudinal coherence length of $0.7 \mu\text{m}$. A set of Kirkpatrick Baez mirrors was used to focus the beam to $1 \mu\text{m}^2$. The rocking curve around the (111) Bragg peak was collected by recording coherent diffraction patterns with a charge coupled device camera around $2\theta = 18 \text{ deg}$ ($\Delta\theta = \pm 0.2 \text{ deg}$). The particle was imaged after an equilibration procedure consisting of a 30-minute holding period at constant voltage followed by 30-minute relaxation to open circuit voltage. After this equilibration procedure, the lattice constant does not change. Three measurements were performed at each charge state and averaged together

6.3.3 Phase Retrieval

The phase retrieval code is adapted from published work and augmented to include GPU capability. 90 iterations of the difference map algorithm [43] followed by ten iterations of the error reduction algorithm [50, 49] were used and the algorithm converged after a total of 3150 iterations. The shrinkwrap algorithm [83] was used to update the support every five iterations. The data set

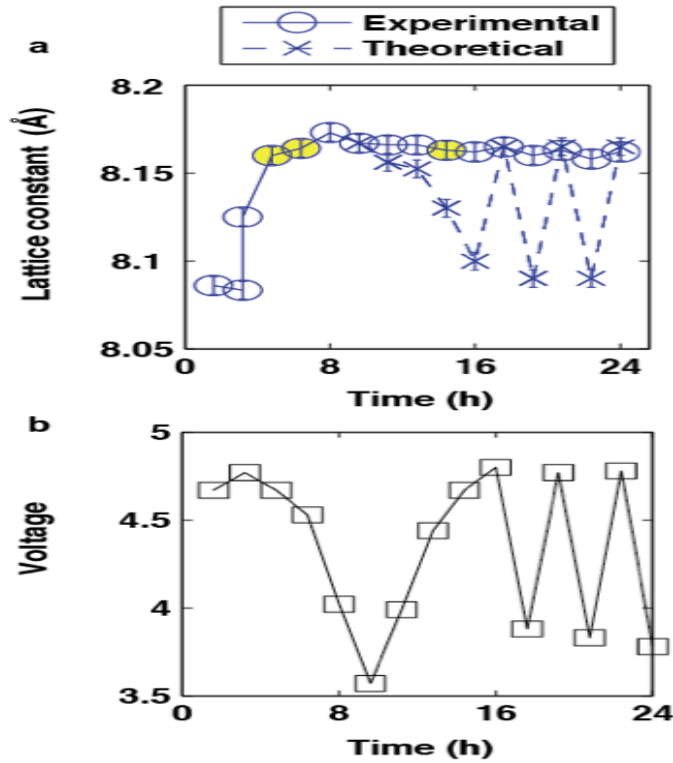


Figure 6.2: Lattice constant evolution during charging and discharging. In Fig. 2a, the measured lattice evolution is shown in blue circles while the evolution for a connected particle during discharge is shown in dashed X. Fig. 2b shows the open circuit voltage at which the measurements were taken.

for each reconstruction is formed by averaging at least 3 independent coherent diffraction measurements taken in succession at the same charge state. At least 10 reconstructions beginning from random phase starts were averaged for the final reconstruction. The final resolution of 40 nm was computed via the phase retrieval transfer function [122].

6.4 Results and Discussion

Figure 6.1 shows schematically the experimental setup. Coherent X-rays from the synchrotron are incident on an in-situ coin cell containing the battery cathode. The coin cell casting had a 5 mm opening, which was sealed with kapton

film on both sides, to transmit X-rays. The windows do not significantly affect the electrochemical performance or the capacity retention as demonstrated by the electrochemical performance in the in-situ coin cell during X-ray exposure [108]. The cathode is approximately 80 microns thick and contains randomly orientated particles as shown by the electron microscopy image. This construction yields well-separated reciprocal space lattice peaks corresponding to individual particles. The particle imaged in this work is octahedral in shape and approximately 600 nm across.

Figure 6.2 shows the average lattice constant of the single particle in blue circles during charging and discharging. The single particle lattice constant is determined by the location of the Bragg peak maximum according to Bragg's law. During discharge (Fig.6.2), the lattice increased as lithium is inserted, as expected [108, 123]. Once fully discharged, the battery is charged and the lattice constant is expected to decrease as lithium is taken out of the particle. However, the lattice constant deviates from connected particle behavior (dashed X values) and only slightly decreases during the charge cycle. The lattice constant changes very little during subsequent cycling between 3.5 V and 5 V after 16 hours. We thus conclude that one or both of the particles' conduction pathways are significantly changed after the 8-hour mark. We note that the battery loses some capacity during each cycle but continues to charge and discharge as expected indicating that most particles are still connected.

In a functional electrode, both electron and ion conductive pathways function such that charge rates such as $C/2$ (30 minutes for full charge) are possible. Ions conduct through the electrolyte while electrons travel through the conductive matrix, carbon black in this specific case, surrounding the cathode particles. Disconnection of one or both of these pathways can happen in several ways. One hypothesis is that the particle lost physical and/or electronic contact with the conductive matrix. The particle did not move more than 400 nm during this measurement due to the 1-micron beam size and 600 nm particle size. The particle could move a fraction of 400 nm, which would be sufficient for disconnection, but it would have to do so while maintaining its exact orientation because the Bragg

reflection was continuously monitored without changing the sample position. The Bragg condition is sensitive to a rotation as small as 10^{-5} radians. Another hypothesis is that the conductive matrix surrounding the particle failed to accommodate the volume changes during cycling and the particle shrunk away losing contact. However, since the disconnection happens after discharge, in which the particle expands, this seems unlikely. In addition, the total volume change is only on the order of 1%. The particle could crack during the phase transformation, but this would most likely affect the orientation of a portion, or all, of the particle and result in a loss of intensity in the Bragg reflection, sensitive to a rotation as small as 10^{-5} radians, which we do not observe. A final hypothesis is that X-ray exposure contributed to the disconnection. However, we successfully imaged multiple particles throughout multiple charge/discharge cycles in three dimensions using the same X-ray dose without observing disconnection. A change in surface chemistry resulting in larger ion impedance could also explain the observed behaviour. The high operating voltage of this cathode makes it particularly susceptible to electrolyte decomposition. Unlike the layer formed at the anode, the so-called solid electrolyte interphase (SEI) layer [94, 10, 143], little is known about the analogous cathode layer [39]. This cathode layer, which could take 1-2 charge-discharge cycles to form, can effectively destroy the ion conduction pathway if the surface species formed are poor ion-conductors and thus limit ion diffusion. Upon closer inspection of Fig. 6.2, the lattice constant does change very slightly in the expected direction after the 8-hour mark. This implies that the particle can still respond but the timescale for ion transport is orders of magnitude slower than before, which is consistent with the formation of a surface layer. We estimate the capacity loss from the first to third cycle at approximately 1.5%. Assuming all capacity loss is due to disconnection of active material this corresponds to the disconnection of 1.5×10^7 particles. 9.85×10^8 particles are still connected.

We further investigated the cause of disconnection by utilizing the full three-dimensional displacement field along [111], $u_{111}(x, y, z)$, to compute the compressive/tensile strain field in this direction, $\partial_{x_{111}} u_{111}$. We computed the strain with respect to the average lattice constant of the particle at the particular charge state

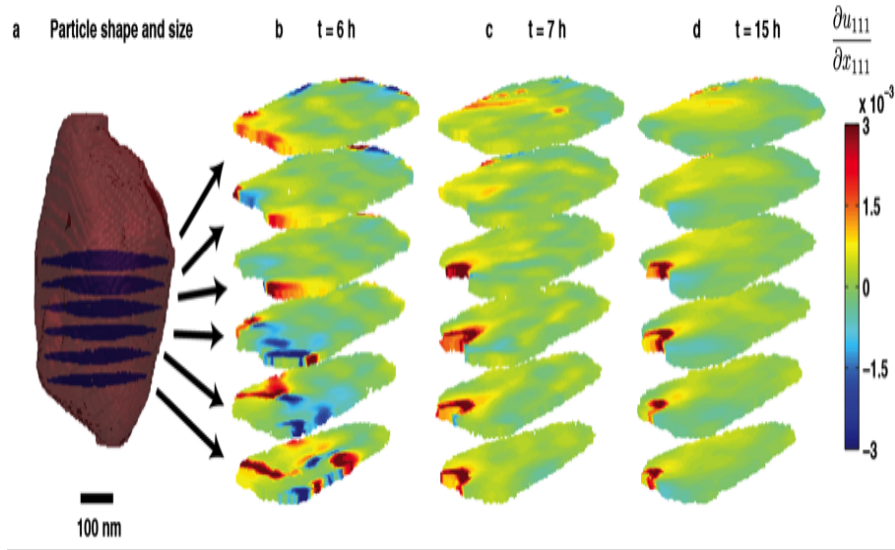


Figure 6.3: 3D Strain evolution throughout the particle during the disconnection event. Compressive/tensile strain maps before and after the disconnection event are shown for 6 cross-sections located throughout the particle as shown in Fig. 6.2.

given by Fig. 6.2. Figure 6.3 shows 6 contour slices of the 3D compressive/tensile strain map at locations indicated by the particle rendering in Fig. 6.3. The three charge states shown correspond to the yellow highlighted points in Fig. 6.2. At $t=6\text{h}$ (Fig. 6.3), large strain exists in both the core and the shell towards the bottom of the particle. This state is in the solid solution regime, so the compressive/tensile strain can be thought of as lithium poor and lithium rich regions, respectively. We thus can see significant lithium inhomogeneity in the bottom 3 contour slices of Fig. 6.3. After the disconnection (Fig. 6.3), a large region of tensile strain still exists in the particle boundary. This could be due to lithium trapped in a cathode electrolyte layer of approximately 50 nm. Figure 6.3 show that the strain map changes only slightly after $t = 7\text{ h}$, which is consistent with a disconnection event and very slow lattice variation as seen in Fig. 6.2. The correlation between lattice constant change and strain field evolution shows that strain evolution is concomitant with lithium concentration changes. The strain field is not significantly governed by interactions with the environment (including neighbouring particles or the electrode) that continue to charge and discharge as

normal. Lithium rearrangement within the particle, which will not change the average lattice constant, on the timescale of the measurement does not occur after 7 hours since the strain field is unchanged. This is consistent with phase field models [34, 13] that show concentration fields are determined by a competition between entropy, enthalpy, and coherency strain. Although the equilibration procedure of a 30-minute hold at constant voltage, followed by a 30-minute relaxation period to open circuit voltage occurs at each point, the particles strain field is essentially unchanged. Lack of detectable changes in the strain field, and by extension ion distribution, within the particle over 10 hours indicate the particle can be considered to be in quasi-equilibrium at all times.

We quantitatively investigate the disconnection event by evaluating the strain field energy. The strain field energy is the sum of the product of the stress and the strain integrated over the particle. Under the assumptions of cubic symmetry and isotropic shear-free conditions in the unit cell, the strain field energy can be simplified [19]

$$E_s = \int (1/2 \sum_{ij} \sigma_{ij} \epsilon_{ij} dV) = (2G + 3I)/2 \int (\partial_{x_{111}} u_{111})^2 dV \quad (6.1)$$

where G and I are the Lamé constants for the material, estimated using molecular dynamics simulations of LiMn_2O_4 spinel [78], and the volume integral is over the entire particle. LNMO always maintains a cubic lattice structure (Figure 5.1) so one strain component is sufficient to evaluate the sum. Elastic strain energy counts the strain due to deviations of the atoms from their equilibrium position, regardless of the underlying cause of the displacement. Figure 6.4 shows the values of the elastic energy, on the order of femtojoules, at different charge states. Initially, the strain energy is relatively low. However, during the structural phase transformation the energy increases more than ten fold, indicating a high amount of strain throughout the particle. This is consistent with structural phase transformations inducing large strains due to the maintenance of coherent interfaces between two phases of different lattice constants [8, 112]. The energy then drops, with a slight modulation upwards before settling at the disconnected value. The fluctuations of the energy thereafter are due to measurement uncertainty, given by the width

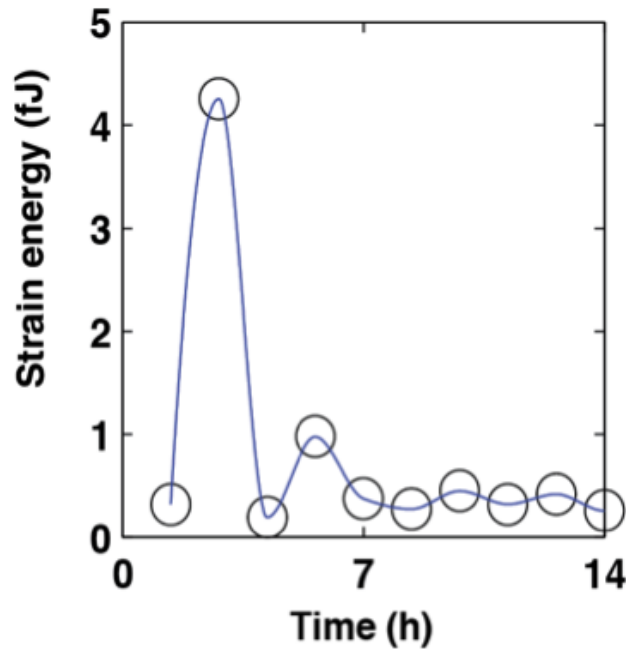


Figure 6.4: Total strain energy (fJ) of the single nanoparticle during charging and discharging. Uncertainty is given by the width of the symbols.

of the symbols, and the very slow variation in the lattice parameter as shown in Fig. 6.2. The values we obtained are consistent with our previous results during discharge [123].

6.5 Conclusions

We revealed in-situ 3D strain evolution of a single cathode nanoparticle during a disconnection event. There are many possible disconnection causes for the particle we image, including particle movement, inelastic response of the conductive matrix, and significant particle cracking. The 3D strain map shows significant lithium inhomogeneity exists near the particle surface, which is consistent with the formation of a poorly conducting surface layer. Electrode engineering is clearly an essential component of improving battery life. Finally, the strain map remains static while the particle is effectively disconnected, indicating the particle is unable to rearrange lithium within the particle volume or exchange lithium with its

neighbours. Thus, strain in this particle is primarily due to Li concentration and not interactions with the surrounding environment. CXDI is thus able to determine the connectivity of single battery nanoparticles, possible reasons for their disconnection, and the equilibrium or non-equilibrium state of single nanocrystals.

6.6 Acknowledgements

This work was supported by U.S. Department of Energy, Office of Science, Office of Basic Energy Sciences, under Contract DE-SC0001805. H.M.C. and Y.S.M. acknowledge the financial support by U.S. Department of Energy, Office of Basic Energy Sciences, under Award Number DE-SC0002357. O.G.S. and Y.S.M. are grateful to the UCSD Chancellors Interdisciplinary Collaborators Award that made this collaboration possible. Use of the Advanced Photon Source, an Office of Science User Facility operated for the U.S. Department of Energy (DOE) Office of Science by Argonne National Laboratory, was supported by the U.S. D.O.E. under Contract No. DE-AC02-06CH11357. A.U. thanks the staff at Argonne National Laboratory and the Advanced Photon Source for their support. J.N.C gratefully acknowledges financial support from the Volkswagen Foundation.

Chapter 6 in full, is a reprint of the material In situ strain evolution during a disconnection event as it appears in *Physical Chemistry Chemical Physics*, Andrew Ulvestad, Jesse Clark, Andrej Singer, David Vine, Hyung-Man Cho, Ross Harder, Ying Shirley Meng and Oleg G. Shpyrko, 2015, 17, 10551. The dissertation author was the primary investigator and author of this paper.

Chapter 7

Topological defect dynamics in *operando* battery nanoparticles

7.1 Abstract

Topological defects can significantly alter nanomaterial properties thereby representing substantial opportunity for defect engineering: the design of desired functionalities through defect manipulation. However, imaging defects in working devices with nanoscale resolution remains elusive. Here we report 3D imaging of dislocation dynamics in individual battery cathode nanoparticles under *operando* conditions using Bragg coherent diffractive imaging. Dislocations are static at room temperature and mobile during charge transport. During the structural phase transformation, the Li-rich phase nucleates near the dislocation and spreads inhomogeneously. The dislocation field is a probe of elastic properties and we find that a region of the material exhibits a negative Poisson's ratio at high voltage. *Operando* dislocation imaging thus opens a powerful avenue for facilitating improvement and rational design of nanostructured materials.

7.2 Introduction

Nanoconfinement causes material properties to differ substantially from their bulk counterparts in many ways, including and can lead to size-tunable thermodynamics, faster intercalation kinetics, and extended life cycles [47]. Defect engineering can be used to further design and optimize properties due to the significant influence of defects on material properties [20, 106]. Motivated by this opportunity, many researchers worked to develop imaging techniques capable of resolving defects, in particular dislocations [68, 98].

The observation of dislocations using techniques such as X-ray topography [99, 116] and reciprocal space mapping X-rays dates back to the 1950s [76, 75, 91]. The coherence of third generation synchrotron X-ray beams enabled several new defect imaging techniques [77], including phase contrast tomography [33] and Bragg X-ray ptychography [115], which was recently used to visualize the displacement field of a dislocation in silicon. For a recent review of defect imaging using coherent methods, see [1]. Bragg coherent diffraction imaging (BCDI), used in this work, relies on interference produced by coherent x-rays and coupled and phase retrieval algorithms to reconstruct the 3D electron density and atomic displacement fields in nanocrystals [31, 125, 123, 136]. The displacement field information BCDI provides is complementary to the aforementioned techniques and crucial in identifying the character of single dislocations. BCDI can also track, with nanoscale resolution, buried single defects under operando conditions thereby accelerating defect engineering in materials for energy storage, conversion, and catalysis.

The role of dislocations in Li-ion battery performance remains largely underexplored, and one of the few areas where materials can be further optimized. On the one hand, the appearance of dislocations correlates with capacity loss [132] as dislocations induce stress and strain. On the other hand, dislocations can relieve strain during phase transformations by allowing the interface between the phases to decohere, and thus prevent cracking and the associated active material loss and undesirable surface reactions with the electrolyte [117, 128]. In order to understand these nuances, we must first track single defects in operating devices under working conditions. Here we use BCDI to study single defects in the nanostructured disor-

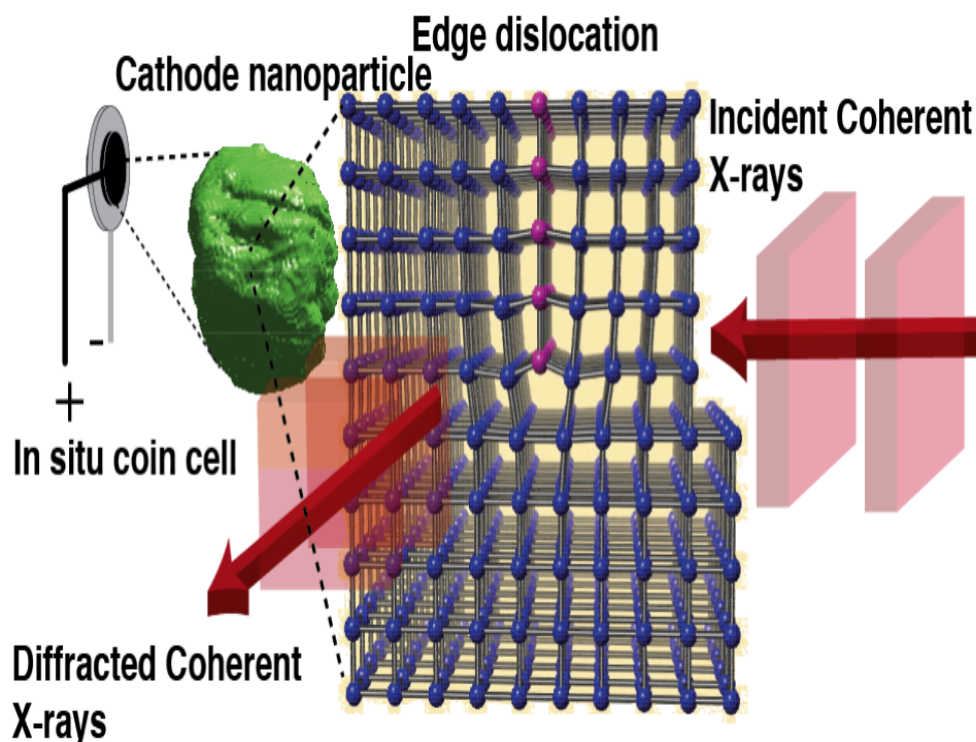


Figure 7.1: Bragg coherent diffractive imaging experiment schematic. Coherent X-rays (red) are incident on a cathode nanoparticle (green).

dered spinel material $\text{LiNi}_{0.5}\text{Mn}_{1.5}\text{O}_4$ (LNMO). LNMO is a promising high voltage cathode material in which the lithium diffusion pathway is three-dimensional [138]. In addition, the material exhibits both two-phase coexistence and phase transformations at certain lithium concentrations during charge and discharge as evidenced by both electrochemical and diffraction data [71, 104, 108, 128]. The phases are different in their lattice constant but have the same symmetry group (Fd-3m).

The experimental setup is shown schematically in Figure 7.1. Focused coherent X-rays are incident on an in-situ coin cell that contains the nanoparticulate LNMO cathode material. The X-rays scattered by a single LNMO particle satisfying the (111) Bragg condition are recorded on an area detector. The experimental geometry combined with the random orientation of the cathode nanoparticles ensures that the (111) Bragg reflections corresponding to separate particles are well separated and an individual reflection can be isolated on the detector. The bat-

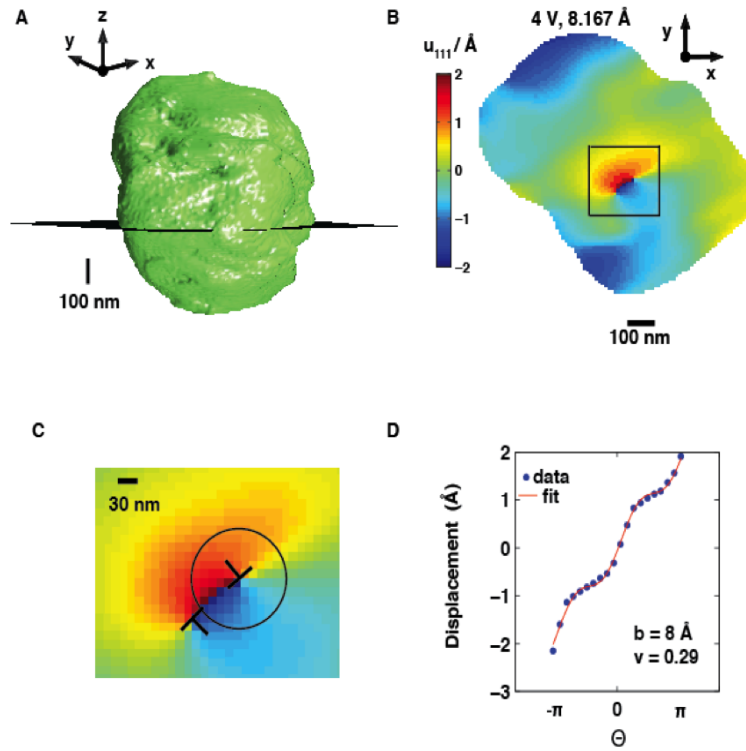


Figure 7.2: Edge dislocation displacement field identified in a single LNMO cathode nanoparticle. Edge dislocations are identified by comparing the measured and predicted displacement field.

tery was cycled 101 times at a fast rate (30 minutes for full charge) prior to the imaging experiment to induce dislocations. From the coherent diffraction data, we reconstruct both the 3D distribution of electron density, $\rho(x, y, z)$, and the 3D displacement field along $[111]$, $u_{111}(x, y, z)$, in an individual cathode nanoparticle.

Figure 7.2 shows a cross-section of the 3D displacement field ($u_{111}(x, y, z = z_0)$) in the cathode nanoparticle. The $[111]$ direction is along the x -axis while the X-ray beam is along the z -axis. To determine the defect type responsible for the displacement field, Fig. 7.2 shows the displacement field magnitudes at a fixed radius, r , as a function of azimuthal angle, θ . Depending on the defect type, this angular distribution will have distinct features. For example, displacement fields generated by screw dislocations must vary linearly with θ [67]. Edge dislocations produce displacements both perpendicular and parallel to the extra half plane

given by [67]

$$u_{\perp} = \frac{b}{2\pi} \left(\theta + \frac{\sin 2\theta}{4(1-\nu)} \right) \quad (7.1)$$

$$u_{\parallel} = -\frac{b}{2\pi} \left(\frac{(1-2\nu)}{4(1-\nu)} \log(r^2) + \frac{\cos 2\theta}{4(1-\nu)} \right) \quad (7.2)$$

where r and θ are the radial and azimuthal coordinate, b is the Burgers vector length and ν is Poisson's ratio. Thus an edge dislocation produces a displacement field that varies linearly with θ with an additional periodic modulation. By inspection of Fig. 7.2, we identify the displacement field as resulting from edge dislocations.

We quantitatively determined the edge dislocation properties and the elastic properties in the nearby region by using Eqs 7.1 with b and ν as fit parameters. Other elastic parameters determined from the displacement field are consistent with expectations. The crystallographic geometry of the edge dislocation with respect to [111] is determined from the 3D displacement field to be 50 ± 8 deg, in good agreement with the predicted value of 54 deg for an edge dislocation along $\langle 100 \rangle$. The fitted Burgers vector magnitude of $8 \pm 1 \text{ \AA}$ is in excellent agreement with the lattice constant along $\langle 100 \rangle$, which is 8.16 \AA , and the fitted Poisson's ratio of 0.27 ± 0.1 agrees with the bulk value of 0.3 in the discharged state [28].

We mapped the edge dislocations in 3D, and by repeated measurements confirmed they were static on the order of an hour at room temperature. Figure 7.3 shows the evolution of the dislocation line as a function of charging. The width of the dislocation line reflects the uncertainty in the position as determined by the phase retrieval transfer function.

Interestingly, we observe dislocation line movement as a function of charge transport, which means the dislocations are stable at room temperature and dynamic under applied current. There is clear inhomogeneity in the amount of movement among different line segments and it does not appear to be random. In fact, there is preferential movement towards the boundary of the particle.

We perform fits as shown in Fig. 7.2 to all dislocations as a function of charge state in order to locally determine the Poisson's ratio in the single particle

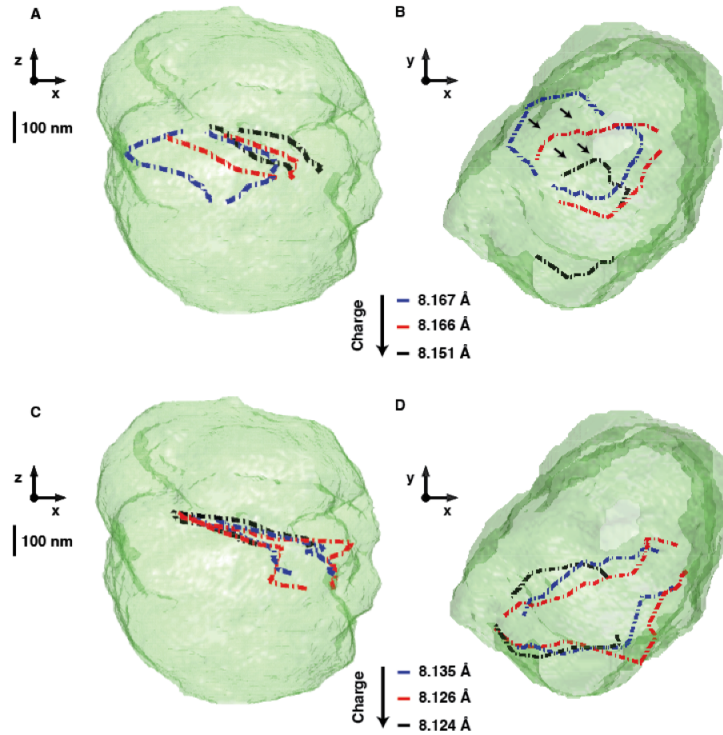


Figure 7.3: 3D Edge dislocation line evolution due to charging. In Fig. 3A, the evolution of the dislocation line at three different charge states is shown. Fig. 3B shows the same evolution as in Fig. 3A for a different view.

along the dislocation line

Figure 7.4 shows Poisson's ratio of the particle in the vicinity of the dislocation line as a function of charge state. At full lithiation (discharged), the local Poisson's ratio is in excellent agreement with the literature value of 0.3 [28]. However, the lithium concentration changes as a function of voltage and is known to change material properties, including Young's modulus [78] and the diffusion coefficient [141]. Surprisingly, here we observe Poisson's ratio decrease during delithiation, eventually becoming negative at roughly 4.5 V.

A possible explanation of the negative Poisson's ratio, or auxetic property, could be due to the peculiar structural changes in LNMO. It is known that materials are auxetic for a variety of reasons, including microstructures, such as re-entrant honeycombs, and due to phase transformations [58]. For example, auxetic

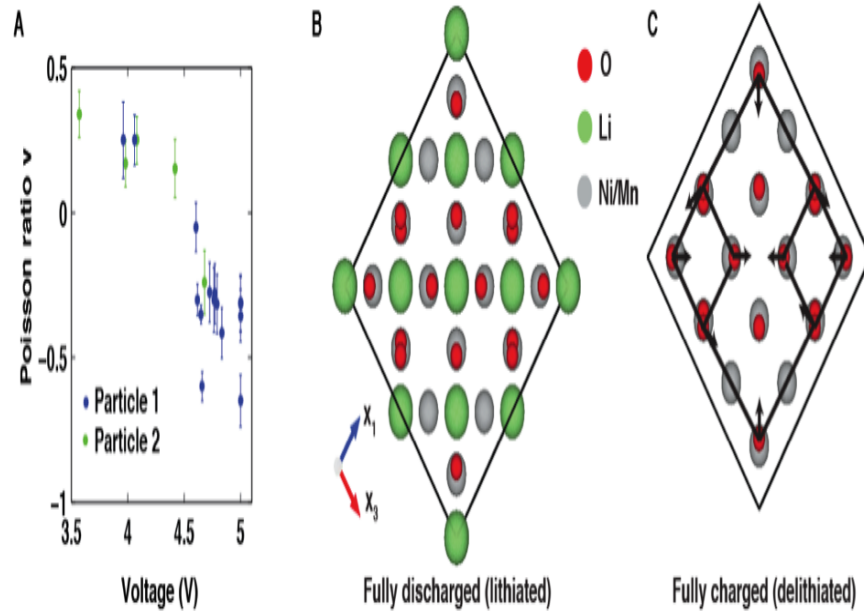


Figure 7.4: The evolution of the local Poisson’s ratio as a function of voltage and the proposed auxetic mechanism occurring in the LNMO unit cell. The proposed auxetic re-entrant honeycomb structure is shown in black in Fig. 4C.

behavior was attributed to a hinge-like structure in spinel CoFe_2O_4 [126], which has the same structure as LNMO. We hypothesize that a hinge-like mechanism as diagrammed in Fig. 7.4 is responsible for the reduction in the measured Poisson’s ratio. At 4.5 V and higher, all of the Mn^{3+} are oxidized to Mn^{4+} , which makes the Mn-O bond exceptionally strong because of the superior ligand field stabilization energy of Mn^{4+} due to its half filled t_{2g} level [138]. This leads to strong and weak bonds within the crystal, and ultimately to the hinge structure. As the voltage is increased and more Lithium is removed, the hinge structure moves more freely and consequently the Poisson’s ratio decreases.

If correct, the delithiated LNMO spinel would be incredibly strain tolerant and have a host of new applications [44], including being used to prevent structural collapse in layered oxide materials at high voltages when blended as a nanocomposite [135]. The auxetic property may also explain why this material is relatively resistant to losing oxygen from the crystal structure at high voltage.

Near 4.7 V, LNMO exhibits two-phase coexistence and a structural phase transformation during charge and discharge as evidenced by both electrochemical and diffraction data [66, 71, 108]. The two phases differ in their lattice constant while the symmetry group of the crystal remains the same. At the single particle level, the phase transformation manifests itself as a splitting in the (111) diffraction peak indicating two lattice constants are present. Figure 7.5 shows the displacement and strain field evolution within the nanoparticle at two measurement times (left and right) corresponding to 4.7 V and 4.69 V during the onset of the phase transformation during discharging. Again, the x-axis corresponds to the [111] direction.

In Fig. 7.5 we qualitatively identify an edge dislocation by inspection of the displacement field. Approximately 20 nm higher, the Li-rich phase nucleated above the dislocation and created tensile strain due to its larger lattice constant. Thus, the observed dislocation is near the phase boundary between the Li-rich and Li-poor phase. From their proximity, we conclude that the dislocation likely acts as a nucleation point for the new phase during the phase transformation, which is expected from theoretical calculations [38]. Interestingly, Figures 5B-C show that further discharge causes the Li-rich phase to expand further into the particle as opposed to nucleating a new phase region a significant spatial distance away. This suggests the near-equilibrium pathway for the phase transformation at the single particle level. The observation of a phase boundary is quite interesting in light of recent results showing the absence of a phase boundary during fast charging in LiFePO_4 [81]. The relatively slow cycling rate (4 hours for full charge) used in this study is most likely responsible for this discrepancy.

7.3 Conclusion

We studied topological defect dynamics in crystalline nanoparticles under operando conditions using Bragg coherent diffractive imaging. We discovered edge dislocations that are static at room temperature and dynamic in response to charge transport. The 3D dislocation displacement field serves as a local probe of elastic

properties and we observe that at high voltage Poisson's ratio in the vicinity of the dislocation is vastly different from that at lower voltages. This calls for further investigation into using lithium ions to tune material properties and could explain why LNMO is resistant to oxygen evolution at high voltage. We anticipate that imaging of dislocations can be used as a nanotechnology to locally probe elastic properties in nanomaterials and that LNMO could improve the strain tolerance of other cathodes. We reconstructed the onset of the phase transformation, observed the dislocation act as a nucleation point, and showed how the phase expands into the particle. Our results open up the imaging of weakly strained phase transformations to BCDI and unlock the potential for a synthesis/imaging feedback loop to engineer dislocations at the nanoscale.

7.4 Acknowledgements

This work was supported by U.S. Department of Energy, Office of Science, Office of Basic Energy Sciences, under Contract DE-SC0001805. HMC and YSM acknowledge the financial support by U.S. Department of Energy, Office of Basic Energy Sciences, under Award Number DE-SC0002357. OGS and YSM are grateful to the UCSD Chancellors Interdisciplinary Collaborators Award that made this collaboration possible. JNC gratefully acknowledges financial support from the Volkswagen Foundation. This research used resources of the Advanced Photon Source, a U.S. Department of Energy (DOE) Office of Science User Facility operated for the DOE Office of Science by Argonne National Laboratory under Contract No. DE-AC02-06CH11357. We thank the staff at Argonne National Laboratory and the Advanced Photon Source for their support. The data is deposited at Sector 34-ID-C of the Advanced Photon Source.

Chapter 7, in full is currently under review for publication of the material Topological defect dynamics in operando battery nanoparticles. Andrew Ulvestad, Andrej Singer, Jesse Clark, Hyung-Man Cho, Jong Woo Kim, Ross Harder, Jorg Maser, Ying Shirley Meng, and Oleg G. Shpyrko. The dissertation author was the primary investigator and author of this paper.

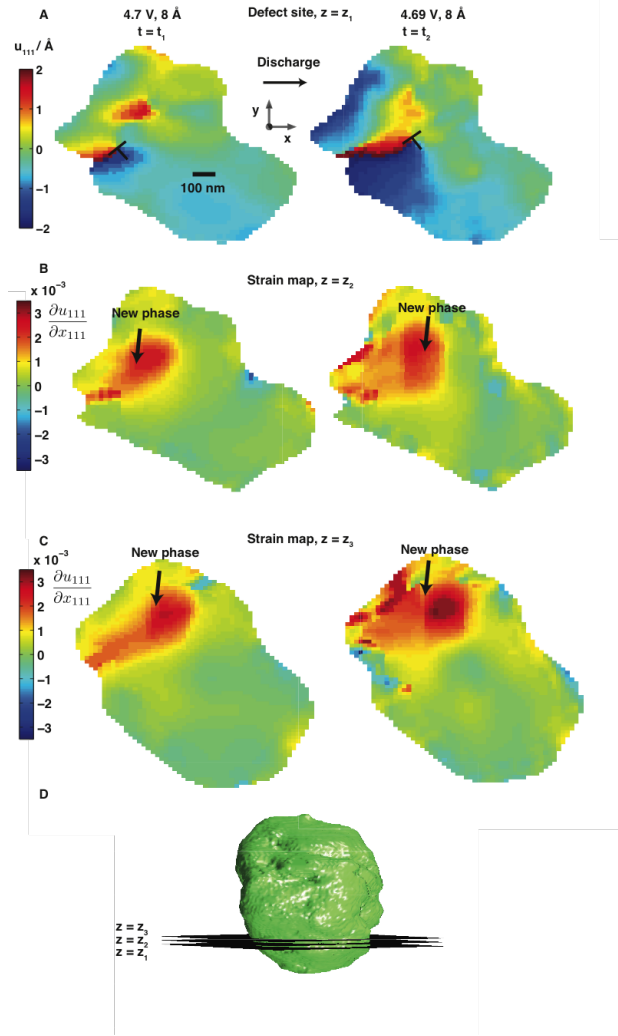


Figure 7.5: Displacement and strain dynamics during the onset of the structural phase transformation. Fig. 5A. shows the edge dislocation. Fig. 5B. shows the time evolution of the strain field in the $[111]$ direction $\partial_{111}u_{111}$ at one cross-section higher than in Fig. 5A. Fig. 5C. again shows strain field evolution.

Chapter 8

Creating universes with thick walls

8.1 Abstract

We study the dynamics of a spherically symmetric false vacuum bubble embedded in a true vacuum region separated by a “thick wall”, which is generated by a scalar field in a quartic potential. We study the “Farhi-Guth-Guven” (FGG) quantum tunneling process by constructing numerical solutions relevant to this process. The “Arnowitt-Deser-Misner” (ADM) mass of the spacetime is calculated, and we show that there is a lower bound that is a significant fraction of the scalar field mass. We argue that the zero mass solutions used to by some to argue against the physicality of the FGG process are artifacts of the thin wall approximation used in earlier work. We argue that the zero mass solutions should not be used to question the viability of the FGG process.

8.2 Introduction

While our universe appears to be well described by Λ CDM cosmology and slow-roll inflation, much about the pre-inflationary universe remains speculative. Numerous models rely on quantum tunneling from some previous state to give an

inflating universe that eventually leads to the universe we observe today (see for example [4]).

We consider here the Farhi-Guth-Guven” (FGG) process which was originally studied in the “thin wall” limit [45],[51]. In this process, a bubble of false vacuum, known as the seed bubble, is separated by a thin domain wall from a region of true vacuum. Einstein’s equation implies two distinct solutions for the motion of the bubble wall; the first eventually collapses while the second expands indefinitely [16]. The possibility of tunneling between these two states is considered. Although FGG consider the case where a seed somehow forms in Minkowski space, other cases were considered (for example in [5]) where the seed forms from Hawking radiation in de Sitter space. Either way, the seed collapses into a black hole but hidden behind the black hole horizon is the expanding solution. The mass of this bubble, M , is the m parameter in the usual Schwarzschild metric, the “ADM” mass.

FGG is known to dominate over Coleman-de Luccia type tunneling[3] and it has been argued that this process can produce inflating universes that do not originate from classical singularities [45, 51, 2]. Despite these features, many calculations that study tunneling in cosmology (for example in the string theory “landscape” [69]) ignore FGG, primarily because of various arguments that this process might not be physical [55, 3]. In this paper we address one of the arguments against the physicality of the FGG process, one that involves taking the bubble mass M to zero[3].

The $M \rightarrow 0$ limit of the thin wall formula leads to a prediction of the FGG process that the probability of transitioning from the seed bubble to the inflating bubble remains finite even as the mass of the seed bubble is taken to zero. This is the ultimate free lunch, since it implies our universe was possibly nucleated from zero matter Minkowski space. However, here we argue that this limit is an artifact of the thin wall approximation which assumes that the thickness of the domain wall is small compared to the radius of the bubble. Indeed, as the radius of the bubble is taken to zero (as it is in the $M \rightarrow 0$ limit), one should expect the thin wall approximation to breakdown.

In this article we examine bubbles of false vacuum separated by a “thick wall”, i.e. scalar field solutions that interpolate between regions of true and false vacuum. We construct numerical solutions for the scalar field coupled to gravity that are relevant to the FGG process. Probably our most important point is an extremely simple one: For a fixed potential the types of possible bubbles are limited and the $M \rightarrow 0$ cannot even be taken. So if one has a particular scalar field potential in mind one is unlikely to encounter the issues raised in [3] about FGG.

In this work we go beyond this simple point by exploring the parameter space of a general quartic scalar field potential (with an overall scale fixed). We find solutions in such potentials cannot approach the step-function type solutions for ϕ that are assumed in the thin wall case, even when the potential is made as “thin wall” as possible. Instead, the scalar field inevitably “spills over” and zero mass solutions are unattainable. By comparison, the thin wall $M \rightarrow 0$ limit relies on exact Schwarzschild space outside the bubble while taking the bubble radius to zero. While it may be possible to find an exotic potential with M arbitrarily small, we show that no quartic potential with a fixed overall scale admits such solutions.

8.3 The thin wall revisited

8.3.1 The setup

Imagine embedding a spherically symmetric bubble of false vacuum, the seed bubble, in a region of true vacuum separated by a domain wall of negligible thickness with surface energy density σ as pictured in Fig. 8.1. The thin wall approximation assumes that the false vacuum is de Sitter space, the true vacuum is Schwarzschild, and the stress energy tensor is discontinuous at the domain wall. Note that we can also allow for a cosmological constant everywhere, and the exterior simply becomes Schwarzschild - de Sitter.

The classical solutions are discussed extensively in [16] and it suffices to repeat a few key results. The mass M of the bubble is the usual Schwarzschild parameter m in the static foliation. This mass can be rewritten as

$$M = \frac{\Lambda^2 r^3}{2G} + 4\pi\sigma r^2 \sqrt{1 + \dot{r}^2 - \Lambda^2 r^2} - 8\pi^2 G \sigma^2 r^3 \quad (8.1)$$

where Λ is the cosmological constant, G is Newton's constant, σ is the surface energy density of the wall, and r is the radial coordinate in the static de Sitter and Schwarzschild foliations. Note that the naive limit $r \rightarrow 0$ appears to give zero mass solutions.

One can use the junction formalism developed in [15]. The basic strategy is to place a coordinate system on the wall and demand continuity of the metric tensor. Then utilizing Einstein's equation, the rescaled radial coordinate, z , obeys the following equation

$$\dot{z}^2 + V(z) = E$$

which is identical to that of a particle moving in a one dimensional potential. We know that if $V > E$, then two solutions exist, but classically the particle cannot move across the barrier. We can, however, have quantum tunneling between the two solutions.

8.3.2 The two solutions

As previously mentioned, two possible solutions exist for the classical motion provided $M < M_{cr}$ where $M_{cr} \sim \Lambda \hat{r}^3$ is the characteristic mass of the problem [16]. Here \hat{r} is the radius of the bubble wall. Type (a) solutions are bounded solutions that begin at $\hat{r} = 0$, expand to some $\hat{r} = r_{max}$ before collapsing back to zero. These solutions avoid a classical singularity, as discussed in FGG, because the trajectory on the Kruskal diagram crosses to the right of the origin and a closed "anti-trapped" surface no longer exists. This point is further elucidated in [2].

Second, there are bounce solutions in which \hat{r} approaches infinity in the asymptotic past, falls to some minimum value, and expands again to approach infinity in the asymptotic future. The Penrose theorem implies that this space-time must have emerged from an initial singularity, since the bubble radius grows beyond $(\Lambda)^{-\frac{1}{2}}$. The way to avoid this classical singularity yet still produce an

inflating universe is to consider tunneling between the two solutions. The two solutions are of identical mass and thus identical energy. This is the FGG process.

The tunneling probability can be calculated using a functional integral [45] or a canonical quantization [51]. In either case, the probability of tunneling between the two solutions remains finite as the mass of the seed bubble, an input parameter, is taken to zero.

8.4 Visiting the thick wall

Consider a scalar field minimally coupled to gravity in a quartic potential, described by the following action

$$S = \frac{1}{2}m_P^2 \int d^4x \sqrt{-g} (R - \nabla_a \phi \nabla_b \phi g^{ab} - 2V(\phi)) \quad (8.2)$$

where $V(\phi) = \lambda\phi^4 - \gamma\phi^3 + \frac{m_i^2}{2}\phi^2$, m_i is the inflaton mass, and m_P is the reduced Planck mass. A particular potential is shown in Fig. 8.2.

We work in a +2 metric signature, in reduced Planck units where $\hbar = 1$, $c = 1$ and $m_P = \sqrt{8\pi G}^{-1}$. One can then nondimensionalize the problem by rescaling the coordinates, for example by using $r^* = rm_P$. This rescales the potential to

$$V(\phi) = \lambda\phi^4 - \gamma\phi^3 + \frac{m_i^2}{2m_P^2}\phi^2$$

Here ϕ , λ and γ are all dimensionless. In what follows, all coordinates and quantities are dimensionless with $m_i = m_P$. Keeping m_i fixed allows us to explore the properties of the bubble solutions without allowing the overall scale of the potential to vanish (in that case one does expect solutions with M approaching zero to be possible). Fixing m_i to the value m_P is convenient for the dynamic range of our numerical work is also a common choice in inflationary models. We use standard spherical, (t, r, θ, ϕ) , coordinates. Under the assumption of spherical symmetry, the spacetime line element takes the form

$$ds^2 = -\alpha^2(r, t)dt^2 + a^2(r, t)dr^2 + r^2d\Omega^2 \quad (8.3)$$

Note that we have not forced the metric in any region to take the de Sitter or Schwarzschild form, although we do require that the spacetime is asymptotically

flat at large r . Here r is both a coordinate and the measure of proper area. The stress-energy tensor of a scalar field in a potential is

$$T_{ab} = \partial_a \phi \partial_b \phi - \frac{1}{2} g_{ab} (\partial_c \phi \partial_d \phi g^{cd} + 2V(\phi)) \quad (8.4)$$

Defining mass in the thick-wall case is more involved, since we no longer have a region of exact Schwarzschild space or a fixed wall position where one can place an observer. Instead, we focus on the ADM mass, which is defined at spatial infinity for asymptotically flat spacetimes. This is the most relevant mass for tunneling calculations [5]. This mass is defined as [27]

$$M = 2\pi \int_0^\infty dr r^2 \left[\left(\frac{\phi'}{a} \right)^2 + \left(\frac{\dot{\phi}}{\alpha} \right)^2 + 2V(\phi) \right] \quad (8.5)$$

where prime denotes differentiation with respect to r while dot denotes differentiation with respect to time.

The tt and rr components of Einstein's equation and the scalar field equation are used to find the turning point. They are listed below. The $\theta\theta$ equation is used as a consistency check.

$$\begin{aligned} 2a^3(r^2V - 1) - 4ra' + a(2 + r^2\phi'^2) &= 0 \\ \frac{2}{r} + a^2(2rV - \frac{2}{r}) + 4\frac{\alpha'}{\alpha} &= r\phi'^2 \\ \frac{a^2}{\alpha^2}(\alpha^2 \frac{dV}{d\phi} - \frac{1}{r^2}) + \frac{a'}{a}\phi' - (\frac{2}{r} + \frac{\alpha'}{\alpha})\phi' &= \phi'' \end{aligned}$$

We use a 4th order Runge-Kutta scheme with adaptive mesh refinement. In true S - dS static spherical coordinates, there is a horizon when $1 - 2m/r - \Lambda/r^2 = 0$. We cannot check this condition a priori, because we do not know the mass of the space-time. However, we check it after and make sure that the computational domain does not include the horizon. Note also that, if there was a horizon inside the computational domain, it would be apparent in the metric functions.

We want to find solutions for a bubble of false vacuum embedded in true vacuum, i.e. we want to find the radial profiles and time evolution of ϕ , α and a . This is done by demanding that $\phi_{r=r_{min}}$ take the value of the false minimum of

the potential, so that $V(\phi_m)$ acts as a cosmological constant near the origin. We also investigated cases in which the scalar field was not initially at the minimum of the potential, which include the extreme case in which $\phi_{r=r_{min}} = \phi_{r=r_{max}} = 0$. In this case, the solution is not just a constant ϕ profile, and so even this solution has some mass.

8.4.1 The turning point

For the purposes of this article it suffices to examine the properties of the classical solutions relevant to the FGG process. There is no need to find the tunneling solutions and the corresponding tunneling actions to make our points. Furthermore, we can understand the relevant properties of these solutions (namely the ADM mass) simply by finding the solution at its turning point, which further simplifies our calculations. At the turning point $\dot{\alpha} = \dot{a} = \dot{\phi} = 0$ but second order time derivatives are nonzero. In this case, equation 8.5 reduces to

$$M = 2\pi \int_0^\infty r^2 \left[\left(\frac{\phi'}{a} \right)^2 + 2V(\phi) \right] dr \quad (8.6)$$

Using Einstein's equation, this can be rewritten as (again setting $m_i = m_P$),

$$M = \frac{4\pi}{3} \int_0^\infty \left(\frac{2ra'}{a^3} - \frac{1}{a^2} + 1 \right) dr$$

so we see that $dm/dr = 0$ only for the Schwarzschild metric, as expected. Additionally, substituting the de Sitter metric into 8.6 gives the energy density times the volume of the bubble, just as one would expect.

Inspection of Eqn. 8.6 (which is positive definite since $V(\phi)$ is everywhere positive) one can see that we do not expect to find $M \equiv 0$ solutions, but there is no apparent reason why a smooth limit to zero should not exist.

There is freedom to specify the spatial profile of $\ddot{\phi}$ at the turning point, which we choose to be $\ddot{\phi} = c/r^2$ for a constant c . This is consistent with spherical symmetry and is sufficiently localized to maintain an asymptotically flat spacetime. Choosing such an ansatz simply enforces locality of the bubble and does not affect the generality of our conclusions.

8.4.2 The two solutions

Evolving forward in time from the turning point solution is used to classify the solution character. The energy density of the expanding solution expands into the domain as the metric functions approach de Sitter (see Fig. 8.3). The energy density of the collapsing solution collapses immediately toward the origin while the metric functions approach pure Schwarzschild. A plot of $T_{00}(t = 0)$, showing the “thickness” of the wall, for the expanding solution is given in figure 8.3. Plots of the field and metric functions for expanding and collapsing solutions are given in figures 8.4 and 8.5, respectively.

8.4.3 Results of trying to take $M \rightarrow 0$

Conceptually, there are two ways in which this can be done. From a cosmological perspective, we can fix the inflaton potential and attempt to take the mass to zero by changing the initial condition on $\ddot{\phi}$.

On the other hand, we can tune the two constants in the potential while keeping a fixed $\ddot{\phi}$. (As discussed and motivated above, we are keeping the overall scale m_i fixed for this investigation.) We begin with a parameter scan over three orders of magnitude, i.e. ranging the values of λ and γ from $0.1 \rightarrow 10$. Let the value of the field at the false minimum and the maximum be ϕ_{min} and ϕ_{max} , and the potential evaluated at these points be V_{min} and V_{max} , respectively. Figures 8.6 and 8.7 show how the mass of the collapsing turning point solution depends on $\Delta\phi = \phi_{min} - \phi_{max}$ and $\Delta V = V_{max} - V_{min}$.

8.5 Discussion

Inspecting Eqn. 8.5, we see that the integrand, dm/dr , will not be zero unless ϕ is constant and $V(\phi) = 0$, i.e. exactly Schwarzschild space. The crux of our argument is that real potentials and fields do not admit nicely separated solutions; the field spills over into the whole domain and affects the metric functions, preventing the $M \rightarrow 0$ limit that appears to exist in the thin-wall formalism.

We still attempted to push the mass smoothly to zero. However, as Figures 8.6 and 8.7 show, we are unable to push the mass below about 0.1. This is with a fixed overall scale set by choosing $m_i = m_P$. The point is not the value of m_i (setting $(m_i/m_P)^2 = 10^{-3}$ does not affect our conclusions), but that we have fixed an overall scale.

In any spherically symmetric problem, there is the issue of what happens at $r = 0$. While the numerics cannot evolve such a point, we can make progress analytically by assuming we approach exact de Sitter space, in which the metric functions are regular at the origin. The scalar field potential can then be expanding about the minimum to second order in ϕ . The problem is then analytically tractable and solutions give positive mass contributions. Thus, our calculation of M really is a lower bound.

8.6 Conclusion

We considered classical solutions relevant to the Farhi-Guth-Guven tunneling process. For a generic quartic potential we are unable to take the mass of our turning point solutions smoothly to zero. Other authors have shown using the thin wall approximation that the FGG tunneling amplitude remains finite as $M \rightarrow 0$, and this strange behavior has been used to question the physicality of the FGG process. The absence of $M \rightarrow 0$ solutions in our more realistic thick wall calculations suggest that the $M \rightarrow 0$ behavior is an artifact of thin wall approximation and should not be used to argue that the FGG process is unphysical.

8.7 Acknowledgements

This work was supported in part by a McCormick Fellowship (AU), and DOE grant DE-FG03-91ER4067 (AA and AU). AA thanks the University of Chicago department of Astronomy and Astrophysics and KICP for hospitality during his sabbatical, when most of this work was completed. We thank Bob Wald and Emil Martinec for fruitful discussions. We also thank A. Aguirre and M. Johnson for

helpful conversations, and the Perimeter Institute, where many of these conversations took place.

Chapter 8 in full, is a reprint of the material *Creating universes with thick walls* as it appears in *Physical Review D*, Andrew Ulvestad and Andreas Albrecht, 2012, 85, 103527. The dissertation author was the primary investigator and author of this paper.

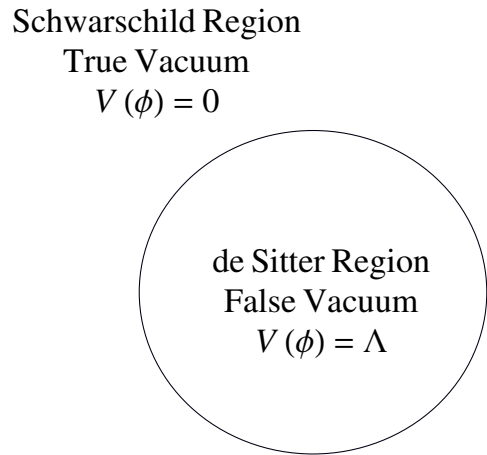


Figure 8.1: A sketch of a bubble solution. A region of de Sitter false vacuum is embedded in a region of true vacuum.

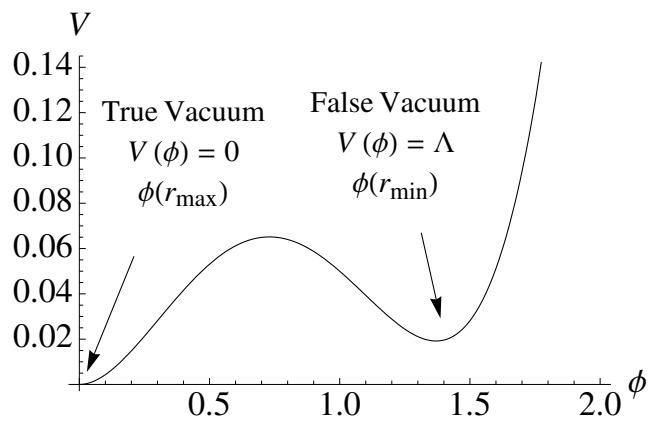


Figure 8.2: A particular ϕ^4 potential with true and false vacuum regions labeled. This potential is used in the numerical solution.

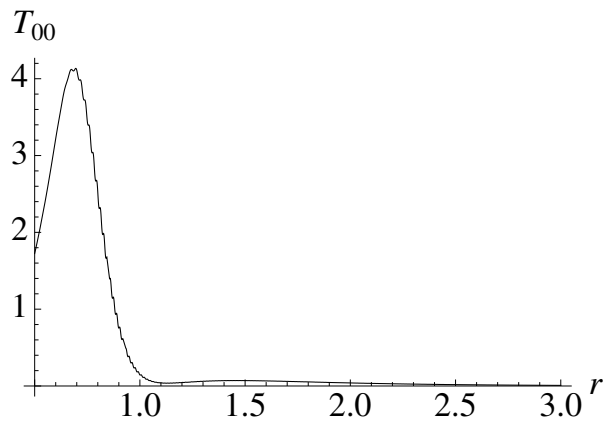


Figure 8.3: T_{00} , a component of the stress energy tensor, demonstrating the wall “thickness”, at a given time.

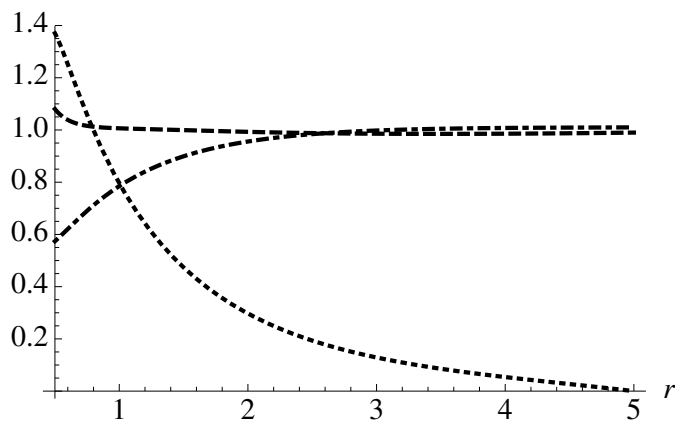


Figure 8.4: Turning point slice of geometry and field for the expanding solution. Here ϕ is dotted, a is dash-dotted, and α is dashed.

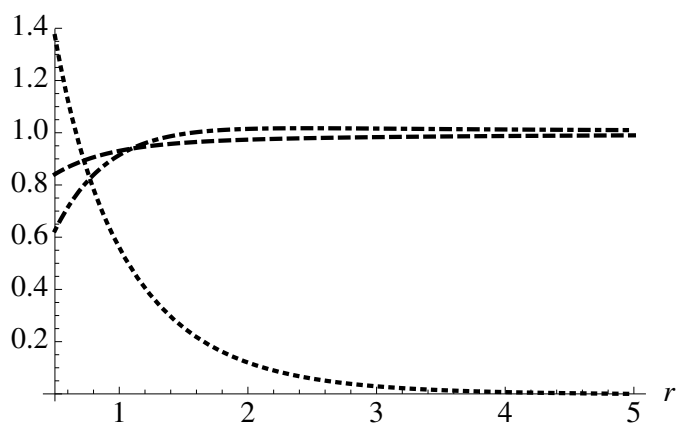


Figure 8.5: Turning point slice of the collapsing solution. Here ϕ is dotted, a is dash-dotted, and α is dashed.

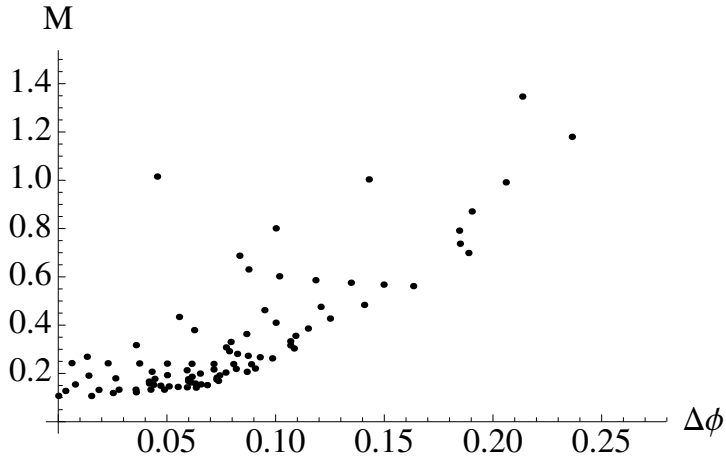


Figure 8.6: Mass of the collapsing solution, evaluated at the turning point, as a function of $\Delta\phi$. Points represent a scan of potential parameters λ and γ . Small values of M were not found in the scan.

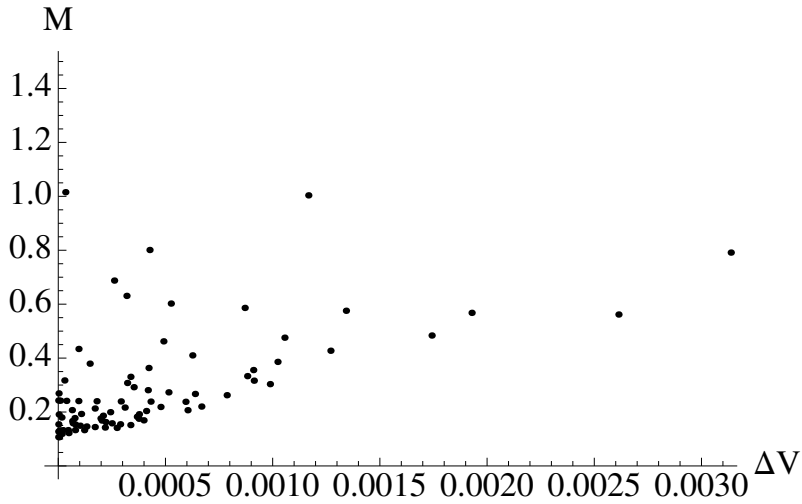


Figure 8.7: Mass of the collapsing solution, evaluated at the turning point, as a function of ΔV . Points represent a scan of potential parameters λ and γ . Small values of M were not found in the scan.

Chapter 9

Conclusions

Engineering of the structure function relationship for nanoparticles represents a considerable opportunity for meeting the grand challenges of our time. The power of nanoparticles lies in the fact that, at the nanoscale, surface effects begin to play an important role in the thermodynamics. For example, surface tension can contract the particle's lattice parameter. The type and degree of faceting can change the charge transfer kinetics. The size of the particle can determine the degree of catalytic activity. There are many more examples and the true promise of nanoparticles in not only physics and materials science, but also in biology, chemistry, and environmental science is only beginning to be realized.

The very promise of nanoparticles makes them difficult to image with traditional techniques. Many techniques average over many particles, require specialized sample environments, provide only 2D information, and/or are insensitive to strain. Electron microscopy produces beautiful images, but tends to be limited to thin samples and specialized sample environments. And yet, without this information, the full promise of nanoparticles is likely to be unfulfilled. Coherent x-ray diffractive imaging is the technique used in this thesis and is particularly adept at resolving both electron density and strain information in 3D under operating conditions for nanoparticles. CXDI is well suited to imaging thick samples immersed in reactive environments. It can also image buried structures such as defects and interfaces. The primary relationship in CXDI is that the scattered intensity is proportional to the Fourier transform of the electron density, and that

asymmetries in this intensity distribution are due to strain in the crystal.

The cathode nanoparticles studied in this thesis undergo a variety of interesting and diverse effects. Strain can be generated from ion intercalation, via the formation of a surface layer, and from defects. The results presented here will allow others to investigate other cathode nanoparticles, including LiFePO_4 and the layered oxide “NCM” materials and the nature of the ion induced strain. The ability to track buried edge dislocations in full 3D detail should find use not only in battery cathode nanoparticles, but also in a host of other applications including semiconductors and solar cells.

The future is very bright for coherent x-ray imaging. The Advanced Photon Source at Argonne National Laboratory is planning to upgrade the coherence properties of the x-ray beam that should result in a factor of around 100 increase in coherent flux. This increase should allow the resolution of the technique to approach the scale of Angstroms. In addition, it will allow the investigation of physics at new time scales. Using current and future sources, coherent x-ray imaging will undoubtedly play a role in the development of next generation materials.

Bibliography

- [1] Brian Abbey. From Grain Boundaries to Single Defects: A Review of Coherent Methods for Materials Imaging in the X-ray Sciences. *JOM*, 65(9):1183–1201, August 2013.
- [2] Anthony Aguirre and Matthew C. Johnson. Dynamics and instability of false vacuum bubbles. *Phys. Rev.*, D72:103525, 2005.
- [3] Anthony Aguirre and Matthew C. Johnson. Two tunnels to inflation. *Phys.Rev.*, D73:123529, 2006.
- [4] Andreas Albrecht. de Sitter equilibrium as a fundamental framework for cosmology. *J. Phys. Conf. Ser.*, 174:012006, 2009.
- [5] Andreas Albrecht and Lorenzo Sorbo. Can the universe afford inflation? *Phys. Rev.*, D70:063528, 2004.
- [6] Jens Als-Nielsen and Des McMorrow. *Elements of modern X-ray physics*. John Wiley & Sons, Inc., 2011.
- [7] AS Andersson and John Oswald Thomas. The source of first-cycle capacity loss in lifepo4. *Journal of Power Sources*, 97:498–502, 2001.
- [8] Antonino Salvatore Aricò, Peter Bruce, Bruno Scrosati, Jean-Marie Tarascon, and Walter van Schalkwijk. Nanostructured materials for advanced energy conversion and storage devices. *Nature materials*, 4(5):366–77, May 2005.
- [9] M Armand and J-M Tarascon. Building better batteries. *Nature*, 451:652–657, 2008.
- [10] P Arora, RE White, and Marc Doyle. Capacity fade mechanisms and side reactions in lithium ion batteries. *Journal of the Electrochemical Society*, 145(10):3647–3667, 1998.
- [11] Pankaj Arora, Ralph E. White, and Marc Doyle. Capacity fade mechanisms and side reactions in lithium ion batteries. *Journal of The Electrochemical Society*, 145(10):3647–3667, 1998.

- [12] Massood Z. Atashbar, Deep Banerji, and Srikanth Singamaneni. Room-temperature hydrogen sensor based on palladium nanowires. *IEEE Sensors Journal*, 5(5):792–797, 2005.
- [13] Peng Bai, Daniel A Cogswell, and Martin Z Bazant. Suppression of phase separation in LiFePO nanoparticles during battery discharge. *Nano letters*, 11(11):4890–6, November 2011.
- [14] N Balke, S Jesse, a N Morozovska, E Eliseev, D W Chung, Y Kim, L Adamczyk, R E García, N Dudney, and S V Kalinin. Nanoscale mapping of ion diffusion in a lithium-ion battery cathode. *Nature nanotechnology*, 5(10):749–54, October 2010.
- [15] V.A. Berezin, V.A. Kuzmin, and I.I. Tkachev. Thin-wall vacuum domain evolution. *Physics Letters B*, 120(13):91 – 96, 1983.
- [16] Steven K. Blau, E. I. Guendelman, and Alan H. Guth. Dynamics of false-vacuum bubbles. *Phys. Rev. D*, 35(6):1747–1766, Mar 1987.
- [17] Vasily V Bulatov, Luke L Hsiung, Meijie Tang, Athanasios Arsenlis, Maria C Bartelt, Wei Cai, Jeff N Florando, Masato Hiratani, Moon Rhee, Gregg Hommes, Tim G Pierce, and Tomas Diaz de la Rubia. Dislocation multi-junctions and strain hardening. *Nature*, 440(7088):1174–1178, 2006.
- [18] Jordi Cabana, Montserrat Casas-Cabanas, Fredrick O Omenya, Natasha A Chernova, Dongli Zeng, M Stanley Whittingham, and Clare P Grey. Composition-structure relationships in the li-ion battery electrode material $\text{LiNi}_{0.5}\text{Mn}_{1.5}\text{O}_4$. *Chemistry of Materials*, 24(15):2952–2964, 2012.
- [19] J Cahn. On spinodal decomposition. *Acta Metallurgica*, 9(9):795–801, 1961.
- [20] Lincoln D Carr and Mark T Lusk. Defect engineering: Graphene gets designer defects. *Nat Nano*, 5(5):316–317, May 2010.
- [21] Kyler J. Carroll, Ming-Che Yang, Gabriel M. Veith, Nancy J. Dudney, and Ying Shirley Meng. Intrinsic Surface Stability in $\text{LiMn}_{2x}\text{Ni}_x\text{O}_{4\delta}$ ($x = 0.45, 0.5$) High Voltage Spinel Materials for Lithium Ion Batteries. *Electrochemical and Solid-State Letters*, 15(5):A72, 2012.
- [22] Candace K Chan, Hailin Peng, Gao Liu, Kevin McIlwrath, Xiao Feng Zhang, Robert a Huggins, and Yi Cui. High-performance lithium battery anodes using silicon nanowires. *Nature nanotechnology*, 3(1):31–35, 2008.
- [23] Henry N Chapman, Anton Barty, Stefano Marchesini, Aleksandr Noy, Stefan P Hau-Riege, Congwu Cui, Malcolm R Howells, Rachel Rosen, Haifeng He, and John CH Spence. High-resolution ab initio three-dimensional x-ray diffraction microscopy. *JOSA A*, 23(5):1179–1200, 2006.

- [24] Di Chen. *Microscopic Investigations of Degradation in Lithium-Ion Batteries*. Thesis, Thesis. Karlsruher Institut für Technologie, 2012.
- [25] Yang-Tse Cheng and Mark W Verbrugge. Diffusion-induced stress, interfacial charge transfer, and criteria for avoiding crack initiation of electrode particles. *Journal of the Electrochemical Society*, 157(4):A508–A516, 2010.
- [26] H.-M. Cho and Y. S. Meng. Effect of Ni/Mn Ordering on Elementary Polarizations of $\text{LiNi}_{0.5}\text{Mn}_{1.5}\text{O}_4$ Spinel and Its Nanostructured Electrode. *Journal of the Electrochemical Society*, 160(9):A1482–A1488, July 2013.
- [27] Matthew W. Choptuik. Universality and scaling in gravitational collapse of a massless scalar field. *Phys. Rev. Lett.*, 70(1):9, Jan 1993.
- [28] John Christensen and John Newman. A Mathematical Model of Stress Generation and Fracture in Lithium Manganese Oxide. *Journal of The Electrochemical Society*, 153(6):A1019, 2006.
- [29] John Christensen and John Newman. A mathematical model of stress generation and fracture in lithium manganese oxide. *Journal of The Electrochemical Society*, 153(6):A1019–A1030, 2006.
- [30] John Christensen and John Newman. Stress generation and fracture in lithium insertion materials. *Journal of Solid State Electrochemistry*, 10(5):293–319, 2006.
- [31] J N Clark, L Beitra, G Xiong, a Higginbotham, D M Fritz, H T Lemke, D Zhu, M Chollet, G J Williams, M Messerschmidt, B Abbey, R J Harder, a M Korsunsky, J S Wark, and I K Robinson. Ultrafast three-dimensional imaging of lattice dynamics in individual gold nanocrystals. *Science (New York, N.Y.)*, 341(6141):56–9, July 2013.
- [32] J N Clark, X Huang, R Harder, and I K Robinson. High-resolution three-dimensional partially coherent diffraction imaging. *Nature communications*, 3:993, January 2012.
- [33] P Cloetens, W Ludwig, E Boller, L Helfen, L Salvo, R Mache, and M Schlenker. Quantitative phase contrast tomography using coherent synchrotron radiation. *Proceedings of the SPIE*, 4503:82–91, 2002.
- [34] Daniel A Cogswell and Martin Z Bazant. Coherency strain and the kinetics of phase separation in LiFePO_4 nanoparticles. *ACS nano*, 6(3):2215–25, March 2012.
- [35] B.D. Cullity. *Elements of X-ray diffraction*. Addison-Wesley metallurgy series. Addison-Wesley Pub. Co., 1956.

- [36] C Delmas, M Maccario, L Croguennec, F Le Cras, and F Weill. Lithium deintercalation in LiFePO₄ nanoparticles via a domino-cascade model. *Nature materials*, 7(8):665–71, August 2008.
- [37] Haixia Deng, Ilias Belharouak, Russel E. Cook, Huiming Wu, Yang-Kook Sun, and Khalil Amine. Nanostructured Lithium Nickel Manganese Oxides for Lithium-Ion Batteries. *Journal of The Electrochemical Society*, 157(4):A447, 2010.
- [38] C.C Dollins. Nucleation on dislocations, 1970.
- [39] Hugues Duncan, Yaser Abu-Lebdeh, and Isobel J. Davidson. Study of the CathodeElectrolyte Interface of LiMn_{1.5}Ni_{0.5}O₄ Synthesized by a SolGel Method for Li-Ion Batteries. *Journal of The Electrochemical Society*, 157(4):A528, April 2010.
- [40] B Dunn, H Kamath, and JM Tarascon. Electrical energy storage for the grid: A battery of choices. *Science*, 334(November):928–935, 2011.
- [41] Bruce Dunn, Haresh Kamath, and Jean-Marie Tarascon. Electrical energy storage for the grid: A battery of choices. *Science*, 334(6058):928–935, 2011.
- [42] Martin Ebner, Federica Marone, Marco Stampanoni, and Vanessa Wood. Visualization and quantification of electrochemical and mechanical degradation in Li ion batteries. *Science (New York, N. Y.)*, 342(6159):716–20, November 2013.
- [43] V Elser, I Rankenburg, and P Thibault. Searching with iterated maps. *Proceedings of the National Academy of Sciences of the United States of America*, 104(2):418–423, 2007.
- [44] Kenneth E. Evans and Andrew Alderson. Auxetic materials: Functional materials and structures from lateral thinking! *Advanced Materials*, 12(9):617–628, 2000.
- [45] Edward Farhi, Alan H. Guth, and Jemal Guven. Is it possible to create a universe in the laboratory by quantum tunneling? *Nuclear Physics B*, 339(2):417 – 490, 1990.
- [46] Christopher R. Fell, Miaofang Chi, Ying Shirley Meng, and Jacob L. Jones. In situ x-ray diffraction study of the lithium excess layered oxide compound Li_{0.2}Ni_{0.2}Mn_{0.6}O₂ during electrochemical cycling. *Solid State Ionics*, 207(0):44 – 49, 2012.
- [47] Maximilian Fichtner. Nanoconfinement effects in energy storage materials. *Physical Chemistry Chemical Physics*, 13:21186, 2011.

- [48] J. R. Fienup. Phase retrieval algorithms: a comparison. *Appl. Opt.*, 21(15):2758–2769, Aug 1982.
- [49] J R Fienup. Phase retrieval algorithms: a comparison. *Applied optics*, 21(15):2758–69, August 1982.
- [50] J. R. Fienup and A. M. Kowalczyk. Phase retrieval for a complex-valued object by using a low-resolution image. *Journal of the Optical Society of America A*, 7(3):450, March 1990.
- [51] W. Fischler, D. Morgan, and J. Polchinski. Quantization of false-vacuum bubbles: A hamiltonian treatment of gravitational tunneling. *Phys. Rev. D*, 42(12):4042–4055, Dec 1990.
- [52] E. Fohtung, J. W. Kim, Keith T. Chan, Ross Harder, Eric E. Fullerton, and O. G. Shpyrko. Probing the three-dimensional strain inhomogeneity and equilibrium elastic properties of single crystal Ni nanowires. *APPLIED PHYSICS LETTERS*, 101(3), JUL 16 2012.
- [53] E.B. Fohtung. *Strain field and strain engineering in semiconductor nanostructures: coherent X-ray diffraction imaging and analytical studies*. PhD thesis, Universitätsbibliothek Freiburg, 2010.
- [54] H Frauenfelder and D T Leeson. The energy landscape in non-biological and biological molecules. *Nature structural biology*, 5(9):757–9, September 1998.
- [55] Ben Freivogel, Veronika E. Hubeny, Alexander Maloney, Robert C. Myers, Mukund Rangamani, et al. Inflation in AdS/CFT. *JHEP*, 0603:007, 2006.
- [56] Lin Gan, Rong Yu, Jun Luo, Zhiying Cheng, and Jing Zhu. Lattice Strain Distributions in Individual Dealloyed PtFe Catalyst Nanoparticles. *The Journal of Physical Chemistry Letters*, 3(7):934–938, April 2012.
- [57] R Edwin Garcia, Yet-Ming Chiang, W Craig Carter, Pimpa Limthongkul, and Catherine M Bishop. Microstructural modeling and design of rechargeable lithium-ion batteries. *Journal of The Electrochemical Society*, 152(1):A255–A263, 2005.
- [58] GN Greaves, AL Greer, RS Lakes, and T Rouxel. Poisson’s ratio and modern materials. *Nature materials*, 10(October):823–838, 2011.
- [59] R.J. Gummow, A. de Kock, and M.M. Thackeray. Improved capacity retention in rechargeable 4 v lithium/lithium-manganese oxide (spinel) cells. *Solid State Ionics*, 69(1):59 – 67, 1994.
- [60] Bin Hai, Alpesh K. Shukla, Hugues Duncan, and Guoying Chen. The effect of particle surface facets on the kinetic properties of $\text{LiMn}_{1.5}\text{Ni}_{0.5}\text{O}_4$ cathode materials. *Journal of Materials Chemistry A*, 1(3):759, 2013.

- [61] Ross Harder and Ian K. Robinson. Coherent X-Ray Diffraction Imaging of Morphology and Strain in Nanomaterials. *Jom*, 65(9):1202–1207, July 2013.
- [62] Masatake Haruta. When gold is not noble: catalysis by nanoparticles. *Chemical record (New York, N.Y.)*, 3(2):75–87, January 2003.
- [63] Tae Wook Heo, Saswata Bhattacharyya, and Long-Qing Chen. A phase field study of strain energy effects on solute-grain boundary interactions. *Acta Materialia*, 59(20):7800–7815, 2011.
- [64] Megan E Holtz, Yingchao Yu, Deniz Gunceler, Jie Gao, Ravishankar Sundararaman, Kathleen a Schwarz, Tomás a Arias, Héctor D Abruña, and David a Muller. Nanoscale imaging of lithium ion distribution during in situ operation of battery electrode and electrolyte. *Nano letters*, 14(3):1453–9, March 2014.
- [65] Jian Yu Huang, Li Zhong, Chong Min Wang, John P. Sullivan, Wu Xu, Li Qiang Zhang, Scott X. Mao, Nicholas S. Hudak, Xiao Hua Liu, Arunkumar Subramanian, Hongyou Fan, Liang Qi, Akihiro Kushima, and Ju Li. In situ observation of the electrochemical lithiation of a single SnO_2 nanowire electrode. *Science*, 330(6010):1515–1520, 2010.
- [66] Robert a Huggins. *Advanced Batteries: Materials Science Aspects*. Springer, 2008.
- [67] D. Hull and D.J. Bacon. *Introduction to Dislocations*. Butterworth-Heinemann, 5th edition, 2011.
- [68] MJ Hÿtch, JL Putaux, and JM Pénisson. Measurement of the displacement field of dislocations to 0.03 Å by electron microscopy. *Nature*, 423(May):270–273, 2003.
- [69] Shamit Kachru, Renata Kallosh, Andrei D. Linde, and Sandip P. Trivedi. De Sitter vacua in string theory. *Phys.Rev.*, D68:046005, 2003.
- [70] A G Khachaturyan. Elastic Strains during Decomposition of Homogeneous Solid Solutions - Periodic Distribution of Decomposition Products. 119, 1969.
- [71] J Kim, S Myung, C S Yoon, S G Kang, and Y Sun. Cathodes Having Two Crystallographic Structures : Fd 3 h m and P 4 3 32. (10):906–914, 2004.
- [72] J.-H. Kim, S.-T. Myung, C. S. Yoon, S. G. Kang, and Y.-K. Sun. Comparative study of $\text{LiNi}_{0.5}\text{Mn}_{1.5}\text{O}_{4-\delta}$ and $\text{LiNi}_{0.5}\text{Mn}_{1.5}\text{O}_4$ cathodes having two crystallographic structures: $\text{Fd}3m$ and $\text{P}4332$. *Chemistry of Materials*, 16(5):906–914, 2004.

- [73] J.-H. Kim, C. S. Yoon, S.-T. Myung, Jai Prakash, and Y.-K. Sun. Phase transitions in $\text{LiNi}_{0.5}\text{Mn}_{1.5}\text{O}_4$ during cycling at 5 v. *Electrochemical and Solid-State Letters*, 7(7):A216–A220, 2004.
- [74] Vladimir Komanicky, Hakim Lddir, Kee Chul Chang, Andreas Menzel, Goran Karapetrov, Daniel Hennessy, Peter Zapol, and Hoydoo You. Shape-dependent activity of platinum array catalyst. *Journal of the American Chemical Society*, 131:5732–5733, 2009.
- [75] A. R. Lang. Direct observation of individual dislocations by x-ray diffraction. *Journal of Applied Physics*, 29(1958):597–598, 1958.
- [76] A. R. Lang and A.P.W. Makepeace. Synchrotron x-ray reticulography : principles and applications. *Journal of Physics D: Applied Physics*, 32:97–103, 1999.
- [77] D. Le Bolloch, S. Ravy, J. Dumas, J. Marcus, F. Livet, C. Detlefs, F. Yakhou, and L. Paolasini. Charge Density Wave Dislocation as Revealed by Coherent X-Ray Diffraction. *Physical Review Letters*, 95(11):116401, September 2005.
- [78] S. Lee, J. Park, a. M. Sastry, and W. Lu. Molecular Dynamics Simulations of SOC-Dependent Elasticity of $\text{Li}_x\text{Mn}_2\text{O}_4$ Spinel in Li-Ion Batteries. *Journal of the Electrochemical Society*, 160(6):A968–A972, April 2013.
- [79] Jia Li, Qihong Fang, Feng Liu, and Youwen Liu. Analytical modeling of dislocation effect on diffusion induced stress in a cylindrical lithium ion battery electrode. *Journal of Power Sources*, 272:121–127, December 2014.
- [80] Xifei Li, Youlong Xu, and Chunlei Wang. Suppression of jahn-teller distortion of spinel LiMn_2O_4 cathode. *Journal of Alloys and Compounds*, 479(12):310 – 313, 2009.
- [81] Hao Liu, J. Owen, A. Hector, and Clare P Grey. Phase-transforming electrodes. *Science*, 344(6191):1451–1452, June 2014.
- [82] R. Malik, a. Abdellahi, and G. Ceder. A Critical Review of the Li Insertion Mechanisms in LiFePO_4 Electrodes. *Journal of the Electrochemical Society*, 160(5):A3179–A3197, May 2013.
- [83] S Marchesini, H He, and HN Chapman. X-ray image reconstruction from a diffraction pattern alone. *Physical Review B*, pages 1–5, 2003.
- [84] Stefano Marchesini, H He, Henry N Chapman, Stefan P Hau-Riege, A Noy, Malcolm R Howells, U Weierstall, and John CH Spence. X-ray image reconstruction from a diffraction pattern alone. *Physical Review B*, 68(14):140101, 2003.

- [85] Y Matsumura, S Wang, and J Mondori. Mechanism leading to irreversible capacity loss in li ion rechargeable batteries. *Journal of the Electrochemical Society*, 142(9):2914–2918, 1995.
- [86] Stefan Meister, SangBum Kim, Judy J Cha, H-S Philip Wong, and Yi Cui. In situ transmission electron microscopy observation of nanostructural changes in phase-change memory. *ACS nano*, 5(4):2742–8, April 2011.
- [87] A. A. Minkevich, T. Baumbach, M. Gailhanou, and O. Thomas. Applicability of an iterative inversion algorithm to the diffraction patterns from inhomogeneously strained crystals. *Phys. Rev. B*, 78:174110, Nov 2008.
- [88] M. Morcrette, Y. Chabre, G. Vaughan, G. Amatucci, J.-B. Leriche, S. Patoux, C. Masquelier, and J-M. Tarascon. In situ x-ray diffraction techniques as a powerful tool to study battery electrode materials. *Electrochimica Acta*, 47(19):3137 – 3149, 2002.
- [89] Gholam-Abbas Nazri and Gianfranco Pistoia. *Lithium batteries: science and technology*. Springer, 2003.
- [90] Johanna Nelson Weker and Michael F. Toney. Emerging In Situ and Operando Nanoscale X-Ray Imaging Techniques for Energy Storage Materials. *Advanced Functional Materials*, pages n/a–n/a, 2015.
- [91] J. B. Newkirk. Method for the detection of dislocations in silicon by x-ray extinction contrast, 1958.
- [92] K. Ozawa. *Lithium Ion Rechargeable Batteries: Materials, Technology, and New Applications*. Wiley, 2012.
- [93] D Pavlov. Premature capacity loss (pcl) of the positive lead/acid battery plate: a new concept to describe the phenomenon. *Journal of power sources*, 42(3):345–363, 1993.
- [94] E Peled. The electrochemical behavior of alkali and alkaline earth metals in nonaqueous battery systems—the solid electrolyte interphase model. *Journal of The Electrochemical Society*, (1):2047–2051, 1979.
- [95] Jess Santos Pea, Izabela Sandu, Olivier Joubert, Flor Snchez Pascual, Carlos Otero Aren, and Thierry Brousse. Electrochemical Reaction Between Lithium and β -Quartz GeO₂. *Electrochemical and Solid-State Letters*, 7(9):A278, 2004.
- [96] M.A. Pfeifer, G.J. Williams, I.A. Vartanyants, R. Harder, and I.K. Robinson. Three-dimensional mapping of a deformation field inside a nanocrystal. *Nature*, 442(7098):63–66, 2006.

- [97] Mark a Pfeifer, Garth J Williams, Ivan a Vartanyants, Ross Harder, and Ian K Robinson. Three-dimensional mapping of a deformation field inside a nanocrystal. *Nature*, 442(7098):63–6, July 2006.
- [98] H. F. Poulsen. *Three-Dimensional X-ray Diffraction Microscopy*. Springer, Berlin, 2004.
- [99] G. N. Ramchandran. X-ray Topographs of Diamond. *Proceedings of the Indian Academy of Sciences*, 19:280–292, 1945.
- [100] I. Robinson and R. Harder. Coherent x-ray diffraction imaging of strain at the nanoscale. *Nature Materials*, 8(4):291–298, 2009.
- [101] Ian Robinson. Nanoparticle Structure by Coherent X-ray Diffraction. *Journal of the Physical Society of Japan*, 82(2):21012, December 2012.
- [102] Ian Robinson and Ross Harder. Coherent X-ray diffraction imaging of strain at the nanoscale. *Nature materials*, 8(4):291–8, April 2009.
- [103] Ian K Robinson. Nanoparticle Structure by Coherent X-ray Diffraction. 82:1–7, 2013.
- [104] Kuppan Saravanan, Angelique Jarry, Robert Kostecki, and Guoying Chen. A study of room-temperature $\text{Li}_x\text{Mn}_{1.5}\text{Ni}_{0.5}\text{O}_4$ solid solutions. *Scientific Reports*, 5(111):8027, 2015.
- [105] David Sayre. Some implications of a theorem due to shannon. *Acta Crystallographica*, 5(6):843–843, 1952.
- [106] Naechul Shin, Miaofang Chi, Jane Y Howe, and Michael a Filler. Rational defect introduction in silicon nanowires. *Nano letters*, 13(5):1928–33, May 2013.
- [107] O G Shpyrko, E D Isaacs, J M Logan, Yejun Feng, G Aeppli, R Jaramillo, H C Kim, T F Rosenbaum, P Zschack, M Sprung, S Narayanan, and a R Sandy. Direct measurement of antiferromagnetic domain fluctuations. *Nature*, 447(7140):68–71, May 2007.
- [108] Andrej Singer, Andrew Phillip Ulvestad, Hyung-Man Cho, Jong Woo Kim, Jorg Maser, Ross Harder, Ying Shirley Meng, and Oleg G Shpyrko. Non-equilibrium structural dynamics of nanoparticles in $\text{LiNi}_{1/2}\text{Mn}_{3/2}\text{O}_4$ cathode under operando conditions. *Nano letters*, August 2014.
- [109] Gogi K Singh, Gerbrand Ceder, and Martin Z Bazant. Intercalation dynamics in rechargeable battery materials: General theory and phase-transformation waves in lifepo₄. *Electrochimica Acta*, 53(26):7599–7613, 2008.

- [110] Gogi K. Singh, Gerbrand Ceder, and Martin Z. Bazant. Intercalation dynamics in rechargeable battery materials: General theory and phase-transformation waves in LiFePO_4 . *Electrochimica Acta*, 53(26):7599–7613, November 2008.
- [111] Y.-K. Sun, C. S. Yoon, C. K. Kim, S. G. Youn, Y.-S. Lee, M. Yoshio, and I.-H. Oh. Degradation mechanism of spinel $\text{LiAl}_{0.2}\text{Mn}_{1.8}\text{O}_4$ cathode materials on high temperature cycling. *Journal of Materials Chemistry*, 11(10):2519–2522, 2001.
- [112] Yang-Kook Sun, Zonghai Chen, Hyung-Joo Noh, Dong-Ju Lee, Hun-Gi Jung, Yang Ren, Steve Wang, Chong Seung Yoon, Seung-Taek Myung, and Khalil Amine. Nanostructured high-energy cathode materials for advanced lithium batteries. *Nature materials*, 11(11):942–7, November 2012.
- [113] Jin Suntivich, Hubert a Gasteiger, Naoaki Yabuuchi, Haruyuki Nakanishi, John B Goodenough, and Yang Shao-Horn. Design principles for oxygen-reduction activity on perovskite oxide catalysts for fuel cells and metal-air batteries. *Nature chemistry*, 3(7):546–50, July 2011.
- [114] Peter V Sushko, Kevin M Rosso, Ji-Guang Zhang, Jun Liu, and Maria L Sushko. Oxygen vacancies and ordering of d-levels control voltage suppression in oxide cathodes: the case of spinel $\text{Li}_{0.5}\text{Mn}_{1.5}\text{O}_4$. *Advanced Functional Materials*, 2013.
- [115] Yukio Takahashi, Akihiro Suzuki, Shin Furutaku, Kazuto Yamauchi, Yoshiki Kohmura, and Tetsuya Ishikawa. Bragg x-ray ptychography of a silicon crystal: Visualization of the dislocation strain field and the production of a vortex beam. *Physical Review B*, 87(12):121201, March 2013.
- [116] B. K. Tanner. *X-ray Diffraction Topography*. Pergamon Press, 1976.
- [117] J M Tarascon and M Armand. Issues and challenges facing rechargeable lithium batteries. Josephson. *Nature*, 414(6861):359–67, 2001.
- [118] T Andrew Taton and David J Norris. Defective promise in photonics. *Nature*, 416(April):685–686, 2002.
- [119] M. M. Thackeray, A. de Kock, M. H. Rossouw, D. Liles, R. Bittihn, and D. Hoge. Spinel electrodes from the limno system for rechargeable lithium battery applications. *Journal of The Electrochemical Society*, 139(2):363–366, 1992.
- [120] Pierre Thibault. ALGORITHMIC METHODS IN DIFFRACTION MICROSCOPY. (August), 2007.

- [121] Ashish Tripathi, Jyoti Mohanty, Sebastian H. Dietze, Oleg G. Shpyrko, Erik Shipton, Eric E. Fullerton, Sang Soo Kim, and Ian McNulty. Dichroic coherent diffractive imaging. *Proceedings of the National Academy of Sciences*, 108(33):13393–13398, 2011.
- [122] Ashish Tripathi, Jyoti Mohanty, Sebastian H Dietze, Oleg G Shpyrko, Erik Shipton, Eric E Fullerton, Sang Soo Kim, and Ian McNulty. Dichroic coherent diffractive imaging. *Proceedings of the National Academy of Sciences of the United States of America*, 108(33):13393–8, August 2011.
- [123] A Ulvestad, H M Cho, R Harder, J W Kim, S H Dietze, E Fohtung, Y S Meng, and O G Shpyrko. Nanoscale strain mapping in battery nanostructures. *Applied Physics Letters*, 073108:2–6, 2014.
- [124] Andrew Ulvestad. Creating universes with thick walls, 2012.
- [125] Andrew Ulvestad, Andrej Singer, Hyung-Man Cho, Jesse N Clark, Ross Harder, Jorg Maser, Ying Shirley Meng, and Oleg G Shpyrko. Single Particle Nanomechanics in Operando Batteries via Lensless Strain Mapping. *Nano letters*, 14:5123–5127, 2014.
- [126] Matjaz Valant, Anna-Karin Axelsson, Frederic Aguesse, and Neil M. Alford. Molecular Auxetic Behavior of Epitaxial Co-Ferrite Spinel Thin Film. *Advanced Functional Materials*, 20(4):644–647, February 2010.
- [127] A. Van der Ven, K. Garikipati, S. Kim, and M. Wagemaker. The Role of Coherency Strains on Phase Stability in $\text{Li}_{x}\text{FePO}_{4}$: Needle Crystallites Minimize Coherency Strain and Overpotential. *Journal of The Electrochemical Society*, 156(11):A949, 2009.
- [128] A Van der Ven, C Marianetti, D Morgan, and G Ceder. Phase transformations and volume changes in spinel $\text{Li}_{x}\text{Mn}_{2}\text{O}_{4}$. *Solid State Ionics*, 135(1):21–32, 2000.
- [129] Georgi N Vayssilov, Yaroslava Lykhach, Annapaola Migani, Thorsten Staudt, Galina P Petrova, Nataliya Tsud, Tomáš Skála, Albert Bruix, Francesc Illas, Kevin C Prince, Vladimír Matolín, Konstantin M Neyman, and Jörg Libuda. catalytically active platinum nanoparticles. *Nature Materials*, 10(4):310–315, 2011.
- [130] J. Vetter, P. Novák, M.R. Wagner, C. Veit, K.-C. Möller, J.O. Besenhard, M. Winter, M. Wohlfahrt-Mehrens, C. Vogler, and a. Hammouche. Ageing mechanisms in lithium-ion batteries. *Journal of Power Sources*, 147(1-2):269–281, September 2005.

- [131] Chong-Min Wang, Xiaolin Li, Zhiguo Wang, Wu Xu, Jun Liu, Fei Gao, Libor Kovarik, Ji-Guang Zhang, Jane Howe, David J Burton, Zhongyi Liu, Xingcheng Xiao, Suntharampillai Thevuthasan, and Donald R Baer. In situ TEM investigation of congruent phase transition and structural evolution of nanostructured silicon/carbon anode for lithium ion batteries. *Nano letters*, 12(3):1624–32, March 2012.
- [132] Haifeng Wang, YI Jang, and Biying Huang. TEM Study of Electrochemical Cycling Induced Damage and Disorder in LiCoO₂ Cathodes for Rechargeable Lithium Batteries. *Journal of The Electrochemical Society*, 146(2):473–480, 1999.
- [133] Moyu Watari, Rachel a McKendry, Manuel Vöggtli, Gabriel Aeppli, Yeong-Ah Soh, Xiaowen Shi, Gang Xiong, Xiaojing Huang, Ross Harder, and Ian K Robinson. Differential stress induced by thiol adsorption on faceted nanocrystals. - SUPPLEMENTAL. *Nature materials*, 10(11):862–6, November 2011.
- [134] J. Nelson Weker, N. Liu, S. Misra, J. C. Andrews, Y. Cui, and M. F. Toney. Insitu nanotomography and operando transmission X-ray microscopy of micron-sized Ge particles. *Energy & Environmental Science*, 7(8):2771, June 2014.
- [135] M Stanley Whittingham. Lithium batteries and cathode materials. *Chemical reviews*, 104(10):4271–301, October 2004.
- [136] GJ Williams, MA Pfeifer, IA Vartanyants, and IK Robinson. Three-dimensional imaging of microstructure in Au nanocrystals. *Physical review letters*, (May):1–4, 2003.
- [137] Jie Xiao, Xilin Chen, Peter V. Sushko, Maria L. Sushko, Libor Kovarik, Jijun Feng, Zhiqun Deng, Jianming Zheng, Gordon L. Graff, Zimin Nie, Daiwon Choi, Jun Liu, Ji-Guang Zhang, and M. Stanley Whittingham. High-performance $\text{Li}_{0.5}\text{Mn}_{1.5}\text{O}_4$ spinel controlled by Mn^{3+} concentration and site disorder. *Advanced Materials*, 24(16):2109–2116, 2012.
- [138] Bo Xu and Shirley Meng. Factors affecting Li mobility in spinel LiMn_2O_4 first-principles study by GGA and GGA+U methods. *Journal of Power Sources*, 195(15):4971–4976, August 2010.
- [139] Bo Xu, Danna Qian, Ziyang Wang, and Ying Shirley Meng. Recent progress in cathode materials research for advanced lithium ion batteries. *Materials Science and Engineering: R: Reports*, 73(56):51 – 65, 2012.
- [140] Atsuo Yamada and Masahiro Tanaka. Jahn-teller structural phase transition around 280K in $\text{LiMn}_{1-x}\text{Ni}_x\text{O}_2$. *Materials research bulletin*, 30(6):715–721, 1995.

- [141] Ming-che Yang, Bo Xu, Ju-hsiang Cheng, Chun-jern Pan, Bing-joe Hwang, and Ying S Meng. Electronic, Structural, and Electrochemical Properties of $\text{LiNi}_x\text{Cu}_y\text{Mn}_{2-x-y}\text{O}_4$ High-Voltage Spinel Materials. *Chemistry of Materials*, 23(11):2832–2841, June 2011.
- [142] Wenge Yang, Xiaojing Huang, Ross Harder, Jesse N Clark, Ian K Robinson, and Ho-kwang Mao. Coherent diffraction imaging of nanoscale strain evolution in a single crystal under high pressure. *Nature communications*, 4:1680, January 2013.
- [143] Yi Zeng, Raymond B. Smith, Peng Bai, and Martin Z. Bazant. Simple formula for Marcus-Hush-Chidsey kinetics. *Journal of Electroanalytical Chemistry*, 735:77–83, December 2014.
- [144] Xiangchun Zhang, Wei Shyy, and Ann Marie Sastry. Numerical simulation of intercalation-induced stress in li-ion battery electrode particles. *Journal of the Electrochemical Society*, 154(10):A910–A916, 2007.
- [145] Jing Zhu, Li Lu, and Kaiyang Zeng. Nanoscale mapping of lithium-ion diffusion in a cathode within an all-solid-state lithium-ion battery by advanced scanning probe microscopy techniques. *ACS Nano*, 7:1666–1675, 2013.